# A General Protocol for Determining the Structures of Molecularly Ordered but Noncrystalline Silicate Frameworks

Darren H. Brouwer,[†] Sylvian Cadars,*[,‡,§] Juergen Eckert,[∥] Zheng Liu,[⊥] Osamu Terasaki,[⊥] and Bradley F. Chmelka*[,‡]

[†]Department of Chemistry, Redeemer University College, Ancaster, Ontario, Canada, L9K 1J4

[‡]Department of Chemical Engineering, University of California, Santa Barbara, California 93106, United States

[§]CEMHTI CNRS UPR3079, Université d'Orléans, 1D, Avenue de la Recherche-Scientifique, 45071 Orléans cedex 2, France

[∥]Department of Chemistry, University of South Florida, 4202 E. Fowler Ave., Tampa, Florida 33620, United States

[⊥]Department of Structural Chemistry, Stockholm University, S-10691 Stockholm, Sweden

Ⓢ *Supporting Information*

**ABSTRACT:** A general protocol is demonstrated for determining the structures of molecularly ordered but noncrystalline solids, which combines constraints provided by X-ray diffraction (XRD), one- and two-dimensional solid-state nuclear magnetic resonance (NMR) spectroscopy, and first-principles quantum chemical calculations. The approach is used to determine the structure(s) of a surfactant-directed layered silicate with short-range order in two dimensions but without long-range periodicity in three-dimensions (3D). The absence of long-range 3D molecular order and corresponding indexable XRD reflections precludes determination of a space group for this layered silicate. Nevertheless, by combining structural constraints obtained from solid-state $^{29}Si$ NMR analyses, including the types and relative populations of distinct $^{29}Si$ sites, their respective $^{29}Si-O-^{29}Si$ connectivities and separation distances, with unit cell parameters (though not space group symmetry) provided by XRD, a comprehensive search of candidate framework structures leads to the identification of a small number of candidate structures that are each compatible with all of the experimental data. Subsequent refinement of the candidate structures using density functional theory calculations allows their evaluation and identification of "best" framework representations, based on their respective lattice energies and quantitative comparisons between experimental and calculated $^{29}Si$ isotropic chemical shifts and $^2J(^{29}Si-O-^{29}Si)$ scalar couplings. The comprehensive analysis identifies three closely related and topologically equivalent framework configurations that are in close agreement with all experimental and theoretical structural constraints. The subtle differences among such similar structural models embody the complexity of the actual framework(s), which likely contain coexisting or subtle distributions of structural order that are intrinsic to the material.
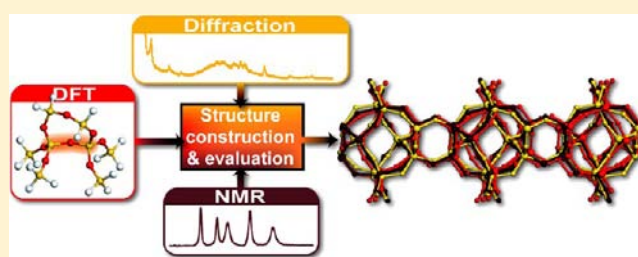
## INTRODUCTION

A molecular-level understanding of the physicochemical properties of crystalline solids generally requires a detailed knowledge of their three-dimensional (3D) atomic structures. X-ray, neutron, and electron diffraction techniques have been, and continue to be, the most important and most commonly used tools for the structure determination of poly- or monocrystalline solids with long-range atomic positional order.[1−3] In recent years, however, solid-state nuclear magnetic resonance (NMR) spectroscopy has emerged as an important complementary tool for the determination of short-range structures of complicated inorganic,[4−14] organic,[15−28] and inorganic−organic host−guest[29−32] or hybrid solids,[33−35] including microcrystalline proteins[36] and materials lacking long-range order.[37−39] Such approaches aim to integrate comprehensively the information provided by solid-state NMR, diffraction, computational chemistry, and other characterization methods into the structure-determination process to improve the robustness, reliability, completeness, and/or accuracy of solid-state structures and the processes by which they are determined.[26,27,40−43]

Molecularly ordered zeolites and layered silicates (e.g., clays) are among the inorganic solids with complicated topologies that have benefited, and continue to benefit, the most from the combination of X-ray diffraction (XRD) and solid-state NMR to characterize their molecular properties and structures. These materials have been extensively studied because of their diverse compositions and rich framework topologies, a number of which exhibit technologically important adsorption, catalytic,[44−47] separation,[48,49] or mechanical properties.[50] Despite their importance, the determination of the molecular structures of these materials has faced a number of challenges. The large majority of zeolites cannot be synthesized as single crystals

large enough to perform single-crystal XRD analyses, leading to reliance on lower-resolution powder analyses that result in less accurate 3D structures. This also applies to layered silicates, which frequently exhibit packing disorder of the sheet assemblies that dramatically complicates the indexing of wide-angle XRD reflections and often prevents the determination of the space group and unit cell parameters. This is particularly true in surfactant-directed layered silicates, which can be synthesized with high degrees of molecular order in their two-dimensional (2D) frameworks but which lack long-range 3D crystallinity.[33,51] These inorganic−organic hybrid solids are of high fundamental and applied interest in materials science.[49,52−54] They exhibit high degrees of order at both the molecular and the mesoscopic length scales, but not in between, which has been challenging to achieve and understand. For the case of self-assembled inorganic-surfactant materials, only a narrow range of synthesis conditions (pH, temperature, surfactant-headgroup hydrophobicity, and solvent composition) lead to the self-assembly of mesostructured inorganic-surfactant composites that subsequently form molecularly ordered silicate sheets separated by flexible surfactant chains.[49,51−53,55]

Solid-state NMR spectroscopy provides important structural information and constraints that open new opportunities for determining the structures of molecularly ordered silicate frameworks.[56−61] In particular, solid-state $^{29}$Si NMR yields: (i) the numbers and relative populations of distinct $^{29}$Si sites in the structure; (ii) the chemical natures of such sites (e.g., the degree of condensation $Q^n$ of four-coordinate $^{29}$Si moieties, where $n$ represents the number of next-nearest-neighbor Si atoms that are covalently bonded via bridging oxygen atoms);[62] (iii) $^{29}$Si−O−$^{29}$Si connectivities among the different resolved sites;[33,63−65] (iv) internuclear $^{29}$Si−O−$^{29}$Si distances;[4,66] and (v) additional local composition and bonding details derived from NMR interactions of $^{29}$Si nuclei (e.g., chemical shift anisotropies[67,68] or scalar couplings[69,70]), including with other nuclei potentially present, e.g., $^{17}$O,[71−74] $^{27}$Al,[75] or $^{23}$Na.[37] Such detailed information provides stringent local structural constraints that can subsequently be combined to determine framework topologies (i−iii), to construct model candidate structures in conjunction with the space groups and unit cell shapes and sizes obtained from XRD data (iv),[4,66] to probe the accuracy of different candidate structures,[69,76] and/or to refine these structures by comparing NMR interactions measured experimentally and calculated from first principles (v).[67,68] Complete structure determination, however, remains a major challenge in non-, semi-, or nanocrystalline solids, where XRD provides little or insufficient information.

Here, we demonstrate a new and general NMR-based structure-determination approach that, in combination with first-principles quantum chemical calculations, establishes the structures of molecularly ordered silicate frameworks that lack long-range 3D atomic crystalline order. This is possible despite the absence of *a priori* information on the space group or atomic coordinates from XRD methods.[33,51] Hedin et al.[33] previously applied the principles of "NMR crystallography," including combined 2D NMR, scattering and molecular modeling analyses, to obtain an approximate structure of a layered silicate framework without long-range molecular order. However, the structural constraints considered in that earlier work, obtained from both experiments and modeling, were insufficient to allow accurate determination of the framework structure. By comparison, our approach here integrates

topological information (e.g., the numbers, relative populations, and connectivities of distinct $^{29}$Si sites) with important new distance and local geometry constraints between $^{29}$Si sites into a general algorithm for comprehensively exploring and evaluating possible framework structures. By applying this general protocol to the challenging case of a molecularly ordered but noncrystalline layered silicate, a set of closely related framework structures is established that accounts for the detailed short-range order of these complicated materials.

## ■ MATERIALS AND METHODS

**Materials.** Surfactant-directed layered silicates with molecularly ordered 1 nm-thick framework sheets were synthesized with natural abundance (4.7%) or enriched (50%) $^{29}$Si, using alkylammonium $CH_3(CH_2)_{15}N^+(CH_3)_2(C_2H_5)$ (abbreviated as "$C_{16}N^+Me_2Et$") surfactant species, as described previously.[33,51] The development of molecular order and resultant structures of the silicate layers arise due to strong interactions between anionic silicate framework moieties and the cationic head groups of the $CH_3(CH_2)_{15}N^+Me_2Et$ surfactant molecules, which cannot be removed without the collapse and disordering of the layered silicate structure. An ammonium-exchanged sample was obtained by contacting the as-synthesized (natural abundance $^{29}$Si) material in a concentrated aqueous solution (28 mol %) of $NH_4OH$ for 24 h under gentle stirring, after which the sample was washed twice with distilled water, vacuum filtered, and dried at 30 °C for 24 h.

**Characterization.** Powder X-ray diffraction (PXRD) patterns were acquired on a Scintag X2 powder diffractometer using Cu $K_\alpha$ radiation (1.54 Å) over a range of $2\theta$ values from 1° to 35° in 0.05° increments. The PXRD pattern of the ammonium-exchanged sample was collected on a Philips XPERT powder diffractometer using Cu $K_\alpha$ radiation (1.54 Å) over a range of $2\theta$ values from 5° to 50° in 0.017° increments.

For the transmission electron microscopy (TEM) measurements, a layered $C_{16}N^+Me_2Et$-silicate sample was synthesized for 12 days at 130 °C and subsequently filtered, washed with deionized water, and air-dried. The sample was ultrasonically dispersed in ethanol (99.9 vol%), and the dispersion subsequently deposited onto a carbon microgrid. High-resolution electron microscopy (HREM) images were acquired using a 400 kV electron microscope (JEM-4000EX) at room temperature.

Solid-state dipolar-mediated $^{29}$Si{$^{29}$Si} double-quantum (DQ) NMR correlation experiments were conducted on a layered silicate-$C_{16}N^+Me_2Et$ sample with $^{29}$Si in natural abundance using a Varian InfinityPlus spectrometer at a magnetic field strength of 7.0 T operating at $^1$H and $^{29}$Si frequencies of 299.85 and 59.56 MHz, respectively. Experiments were conducted at room temperature under magic-angle-spinning (MAS) conditions at 3200 ± 2 Hz using a 6 mm MAS probehead with rotors holding ∼200 mg of sample. The 2D dipolar-mediated $^{29}$Si{$^{29}$Si} DQ NMR correlation experiments used the robust symmetry-based SR26$_4^{11}$ homonuclear dipolar recoupling sequence,[77] as described in previous work on siliceous zeolites.[4,77] A series of 2D $^{29}$Si{$^{29}$Si} DQ correlation spectra were acquired with recoupling times between 2.5 and 35 ms and were collected over a period of 7 days (18 h per 2D experiment).

1D $J$-mediated $^{29}$Si{$^{29}$Si} DQ NMR measurements of $^{29}$Si scalar ($J$) couplings involving covalently bonded $^{29}$Si−O−$^{29}$Si pairs of atoms were performed using the $z$-filtered in-phase−antiphase (IPAP) experiment[78] on a Bruker AVANCE-300 wide-bore NMR spectrometer at 7.0 T operating at $^1$H and $^{29}$Si frequencies of 300.12 and 59.62 MHz, respectively. The experiments were conducted on an otherwise identical layered silicate-$C_{16}N^+Me_2Et$ sample that was enriched in $^{29}$Si to 50%, using a 2.5 mm double resonance MAS probehead and using MAS conditions of 12 kHz (±10 Hz). Recent measurements of $^2J(^{29}$Si−O−$^{29}$Si) couplings conducted on similar layered silicate−surfactant materials with 50% $^{29}$Si enrichment demonstrated that the $z$-filtered IPAP technique permitted NMR signals from distinct $^{29}$Si sites to be manipulated independently.[78] This is achieved through use

5642

dx.doi.org/10.1021/ja311649m | *J. Am. Chem. Soc.* 2013, 135, 5641−5655

of frequency-selective rf pulses (long low-power pulses that selectively excite a narrow region of the spectrum) to measure separately the scalar couplings associated with the specific $^{29}Si(i)-O-^{29}Si(j)$ spin pairs. Total experimental durations varied between 2 and 11 h, depending on the $^{29}Si-O-^{29}Si$ spin pair selected among the different sites. Experimental uncertainties related to the accuracies of the 2D spectral intensities obtained for each $\tau$ increment of the $^{29}Si$ J-coupling spin−echo modulation were assumed to be equal to twice the standard deviation of the best fit. This corresponds to fluctuations of the detected $^{29}Si$ signals of $\pm 2-5\%$ of the intensity of the first increment, which may be due to a combination of spinning instabilities ($\pm 10$ Hz) or thermal effects. Uncertainties related to the measured $^{2}J(^{29}Si-O-^{29}Si)$ couplings, enrichment level $\alpha$, and transverse dephasing times were calculated using covariance matrices,[79,80] with errors of the measured intensities taken as twice their respective standard deviations to each best fit. Uncertainties resulting from the effects of a small misset of the magic angle (adjusted to an estimated precision of $\pm 0.1°$ by minimizing the$^{79}Br$ MAS line width of KBr) were investigated and found to be negligible. More detailed information on the NMR measurements and analyses are included in the Supporting Information (SI).

**Structure Construction-and-Evaluation Procedure.** Structural models for the silicate layer were constructed from solid-state dipolar-mediated $^{29}Si\{^{29}Si\}$ DQ NMR data, and the unit cell parameters provided by PXRD using a recently developed extension of a method for solving the crystal structures of zeolites[66] even without knowledge of the symmetries of their crystallographic space groups. This structure-determination algorithm is described and explained in detail in ref 81. Briefly, the method involves building candidate structures one atom at a time and evaluating the partial candidate structures at each step according to their agreement with $^{29}Si-O-^{29}Si$ connectivity information, equivalence of local structures for atoms of the same type of Si site within the unit cell, and quality of fit to the $^{29}Si\{^{29}Si\}$ DQ buildup curves. These structural constraints are integrated into a parameter $R_{DQ}$ that describes the overall quality of the collective fits to the $^{29}Si\{^{29}Si\}$ DQ curves, as defined and discussed in the SI. The structure construction-and-evaluation algorithm was implemented in Mathematica version 6.0.[82]

**First-Principles Calculations.** Density functional theory (DFT) calculations with periodic boundary conditions were performed with the CASTEP code,[83,84] which uses a plane-wave-based DFT approach. The electron correlation effects were modeled using the PBE generalized gradient approximation,[85] and so-called "on-the-fly" ultrasoft pseudopotentials were employed for all atoms.[86] Geometry optimizations were carried out in frozen cells with a cutoff energy of 700 eV and a $3 \times 4 \times 1$ Monkhorst−Pack[87] (MP) grid to sample the Brillouin zone. These conditions lead to energies converged within <0.02 eV on model silicate systems (e.g., quartz). Layered silicate structures used unit cells with a reduced $c$-parameter of 17.5 Å in the absence of surfactant molecules, with dimensions of (8.5, 6.8, 17.5 Å) and (90, 90, 90°) or (9.10, 7.28, 17.5 Å) and (90, 90, 111°). Symmetry was imposed during geometric optimization for structures within the $P\bar{1}$ space group. The calculations of NMR shielding values were performed using the Gauge Including Projector Augmented Wave approach (GIPAW),[88,89] at the cutoff energy of 600 eV, and using a $3 \times 4 \times 2$ MP grid. Convergence of calculated $^{29}Si$ NMR parameters was tested on quartz and found to be achieved within <0.1 ppm for these conditions. To compensate for possible systematic errors in the absolute values of the $^{29}Si$ shieldings calculated by DFT, $^{29}Si$ chemical shifts were computed for a series of crystalline silicates with known structures and known experimental $^{29}Si$ chemical shifts relative to TMS, against which unknown structures could be calibrated. Table S1 summarizes the reference silicates examined, their respective experimentally measured isotropic $^{29}Si$ chemical shifts and calculated $^{29}Si$ shieldings for distinct framework sites, along with the calculation protocol used. By comparing the calculated and experimentally measured values of the isotropic $^{29}Si$ chemical shifts for the crystalline reference silicates (for which high quality structures are assumed), an uncertainty of $\pm 0.5$ ppm is estimated for the calculated $^{29}Si$ shift values.

DFT calculations of $^{2}J(^{29}Si-O-^{29}Si)$ couplings were carried out using Gaussian 03 (ref 90) and the (pure DFT) PBE functional[85] after thorough tests performed on siliceous zeolites Sigma-2 and ZSM-12, some of which have been reported in ref 69. Scalar couplings were calculated within the GIAO[91] approximation, using locally dense basis sets with Jensen's pcJ-3 basis sets[92] specifically optimized for J-coupling calculations (obtained from the EMSL basis set exchange database)[93,94] on coupled $^{29}Si$ atoms, and using a 6-31++G* basis set augmented with diffuse functions on other atoms. Calculations were performed on small O-centered SiH-terminated clusters containing between 6 and 8 Si atoms, 7 or 8 O atoms, and between 12 and 18 H atoms, depending on whether or not the coupled $^{29}Si$ nuclei were part of four-member rings, respectively; terminal H atoms were placed so as to form Si−H bonds aligned with the Si−O bond being replaced, with a Si−H distance of 1.48 Å. This cluster definition was found to yield errors on calculated couplings of $< \pm 1$ Hz with respect to (considerably more involved) calculations performed on larger OH-terminated clusters, provided appropriate locally dense basis sets were used.[69] Calculations were conducted using the GridChem cyber-infrastructure for computational chemistry,[95−97] at the PSMN, at the Ecole Normale Supérieure de Lyon and at the Centre de Ressources Informatiques de Haute-Normandie (CRIHAN).

## RESULTS AND DISCUSSION

**Ordering over Discrete Length Scales.** Surfactant-directed layered silicates exhibit 2D molecular order in their frameworks, with liquid-crystal-like order (and disorder) over mesoscopic dimensions (~5−10 nm). As shown in Figure 1,
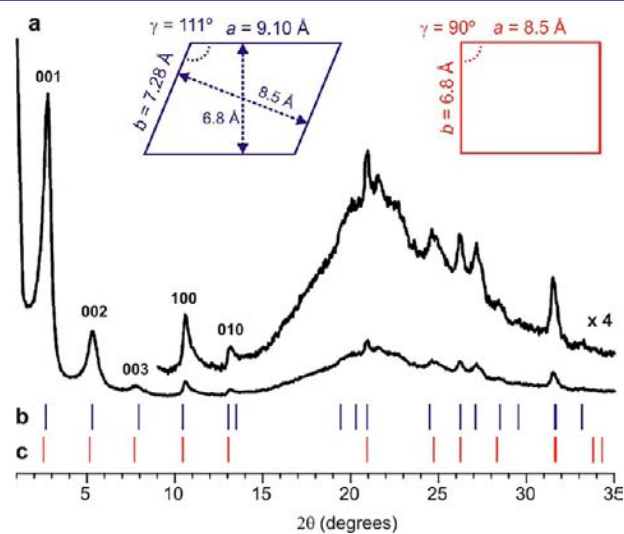


**Figure 1.** (a) PXRD pattern of a layered silicate-$C_{16}N^{+}Me_2Et$ surfactant mesophase with a molecularly ordered silicate framework. (b,c) Calculated (001), (002), (003), and (hk0) reflection positions are shown for layered silicate structures with in-plane unit cells in the insets: (blue) $a = 9.10$ Å, $b = 7.28$ Å, $c = 33.5$ Å, $\gamma = 111°$ and (red) $a = 8.5$ Å, $b = 6.8$ Å, $c = 34.6$ Å, $\gamma = 90°$. The lines indicate the positions of the calculated reflections, regardless of their intensities. Only (hk0) reflections were calculated, because those with $l > 0$ are expected to be broadened due to the lack of coherent scattering between the silicate layers that lack transverse registry with each other.

the PXRD pattern of a layered $C_{16}N^{+}Me_2Et$-silicate material[33,51] consists of a relatively small number of broadened, yet distinct, reflections that overlay much broader intensity. The three small-angle reflections at $d$-spacings of 34.6, 17.4, and 11.5 Å are attributed to the (001), (002), and (003) reflections that are characteristic of lamellar mesostructural order, the first of which reflects the uniform basal spacing (34.6 Å distance

between silicate layers). The reflections at higher angles, such as at $d$-spacings of 8.5 and 6.8 Å, have been attributed to (100) and (010) reflections that arise from periodicity *within* the ordered silicate layers.[51] They indicate that the material has a modest degree of long-range molecular order parallel to the sheets, though without the long-range 3D atomic periodicity that manifests a fully crystalline material. Reflections of the form ($h0l$), ($0kl$), and ($hkl$) with $h$, $k$, and $l \neq 0$ are expected to be absent from this diffraction pattern, because of translational and rotational disorder between adjacent layers, as observed in other molecularly ordered layered systems, where adjacent layers are separated by similarly long and flexible surfactant molecules.[52]

From these observations, and an assumption that the angle $\gamma$ between the $a$ and $b$ axes was 90°, it was concluded previously[33,51] that the $C_{16}N^+Me_2Et$-silicate framework consisted of ordered 1 nm thick silicate layers with unit cell parameters of $a = 8.5$ and $b = 6.8$ Å and that these layers were separated from one another by $c = 34.6$ Å, with all angles between the various unit cell directions being 90° (Figure 1, red inset). The calculated reflection positions based on these lattice parameters (red vertical lines in Figure 1c) show agreement with most of the observed reflections, although on closer inspection there are several that are predicted but which are not present in the experimental XRD pattern (e.g., those near $2\theta$ values 34°). In addition, there are several observed reflections that are not accounted for in the calculated XRD pattern (e.g., the weak reflections near 20° and 33° and the strong reflection at 27°). By considering these higher angle reflections and allowing the $\gamma$ angle between the $a$ and $b$ axes to vary, an improved set of unit-cell lattice parameters is found with $a = 9.10$ Å, $b = 7.28$ Å, $c = 33.5$ Å and $\gamma = 111°$ (Figure 1, blue inset). This is evidenced by improved agreement of the calculated reflections (blue vertical lines in Figure 1b) with the reflection positions in the PXRD pattern, including the $d$-spacings at 8.5 and 6.8 Å. (Changing $c$ to 33.5 Å from 34.5 Å also yielded improved agreement with the positions of the first three reflections arising from the interlayer spacing.) The only discrepancy is in the $2\theta$ region near 22°, which is likely due to the maximum of the broad "amorphous" background signal upon which these sharper reflections are superimposed and which is largely due to diffraction intensity from the disordered surfactant moieties (as established from separate neutron diffraction measurements, not shown here). These results are corroborated by separate PXRD and $^{29}$Si MAS NMR analyses (Figures S1, S2, and S3) of an otherwise identical layered silicate material in which the surfactant species and/or solvent molecules were exchanged with ammonium ions, resulting in narrower and better defined reflections at positions identical to those of the original $C_{16}N^+Me_2Et$-silicate material.

Beyond establishing the layered mesostructure and an estimate of the unit cell parameters, however, there is little else that can be concluded from the PXRD pattern. The poorly resolved reflections do not allow the symmetry of the structure (i.e., space group) to be obtained, and it is not possible *a fortiori* to derive a structural model based on the PXRD data alone. XRD-based structure solutions and refinements are based not only on reflection positions but also on their intensities, which are dramatically modified by the large extent of stacking disorder and the relatively short-range molecular order within the silicate sheets.

High-resolution transmission electron microscopy (TEM) corroborates the high degrees of mesoscopic and molecular
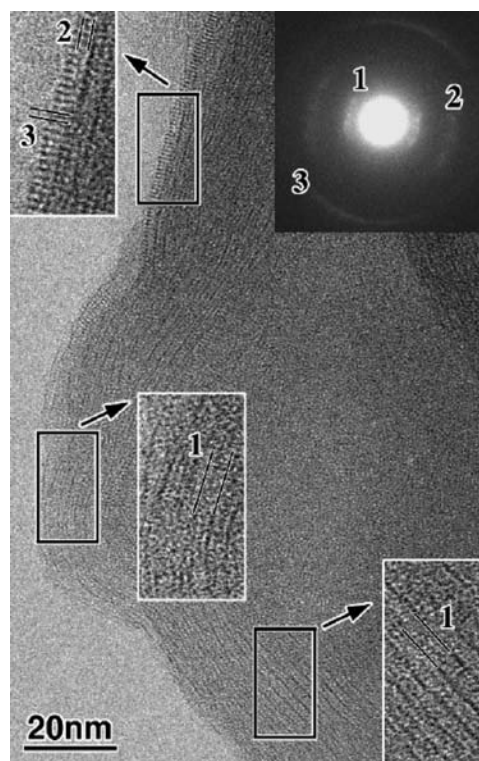


**Figure 2.** High-resolution transmission electron micrograph of a representative region of a surfactant-directed layered silicate-$C_{16}N^+Me_2Et$ particle. The corresponding, and correctly oriented, ED pattern is shown in the upper right-hand corner. The numbered reflections "1", "2", and "3" in the ED pattern correlate with the distances between (001), (002), and (100) planes observed in the TEM image, which are more clearly seen in the enlarged inset regions.

order of the layered silicate-$C_{16}N^+Me_2Et$ material. Figure 2 shows a TEM image and corresponding electron diffraction (ED) pattern of a layered silicate-$C_{16}N^+Me_2Et$ particle, providing imaging evidence of molecularly ordered framework atoms. Three different planar distances are clearly observed in the TEM image and the ED pattern, manifested by the three characteristic lengths and spotty arcs labeled "1", "2", and "3" in Figure 2. The interplanar distances calculated from the ED pattern and the TEM image at locations "1", "2", and "3" are 26, 13, and 9 Å, respectively. The scattering intensities at 26 and 13 Å are consistent with the (001) and (002) reflections associated with the lamellar mesoscale organization of the material.[98] The scattering intensity at 9 Å ("3") cannot be assigned to the ($00l$) reflection, because in the 2D ED pattern it appears in a different diffraction plane than that common to reflections "1" and "2". In addition, the reflection at 9 Å is substantially sharper and agrees well with the narrow PXRD reflection at a $d$-spacing of 8.5 Å (Figure 1) that is attributed to intrasheet framework order. However, little if any additional information can be extracted from the TEM data with regard to more specific ordering of the atoms within the layered silicate framework. The TEM, ED, and XRD results thus corroborate ordering over mesoscopic and molecular length scales in the layered silicate-$C_{16}N^+Me_2Et$ material. However, they are insufficient for determining more precise structural details, because of the limited extent of long-range molecular order even parallel to the sheets, due at least in part to the curvature of the layers revealed by the TEM image in Figure 2.
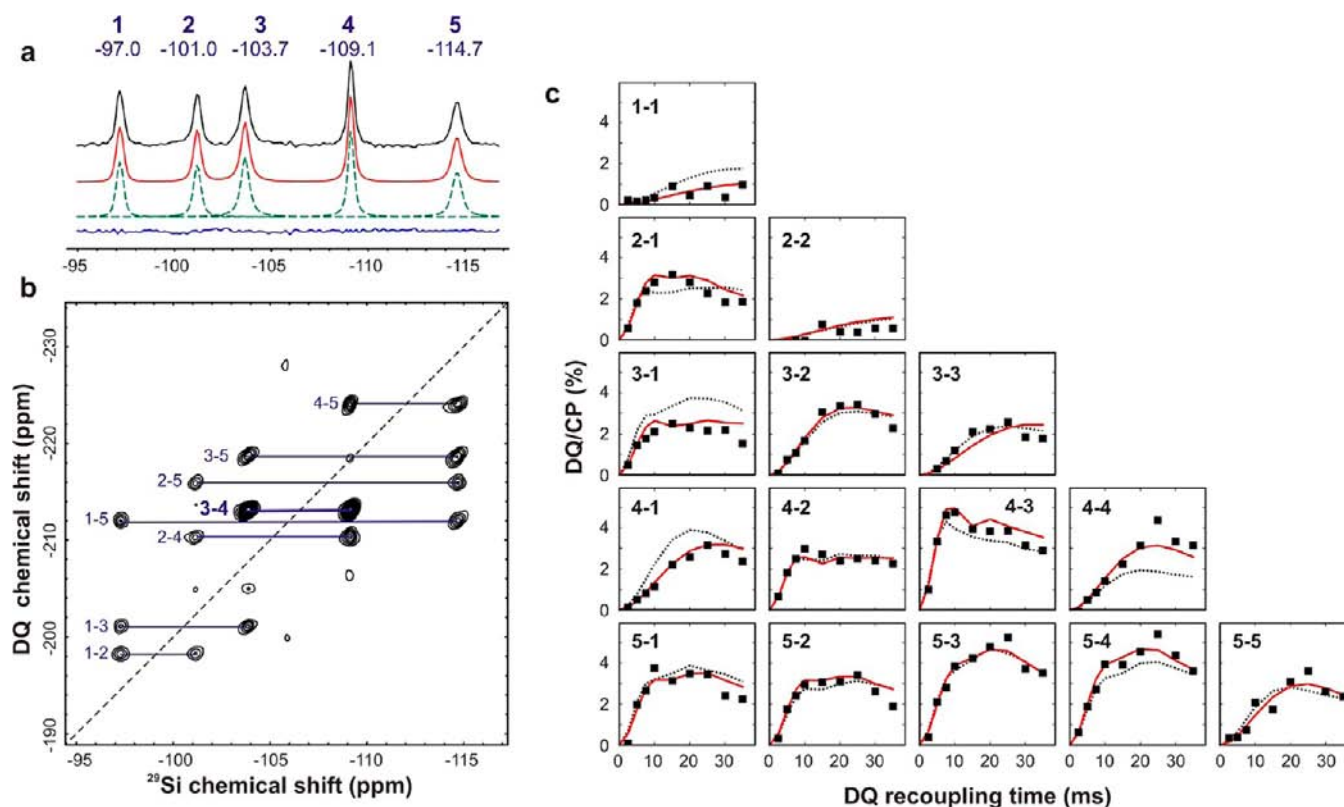
**Figure 3.** Solid-state $^{29}$Si NMR results for the layered silicate-$C_{16}N^+Me_2Et$ surfactant mesophase with a molecularly ordered silicate framework, whose XRD pattern is shown in Figure 1: (a) 1D $^{29}$Si$\{^1H\}$ CP-MAS NMR and simulated spectra, from top to bottom: experimental spectrum (black), overall calculated spectrum (red), individual peaks (green dashed) calculated with equal peak areas, and difference spectrum (blue). (b) 2D $^{29}$Si$\{^{29}Si\}$ dipolar-mediated DQ correlation spectrum acquired with a recoupling time of 5 ms. (c) $^{29}$Si$\{^{29}Si\}$ DQ-intensity buildup curves constructed from experimental data (black squares) obtained by integrating the correlated signals in a series of 2D $^{29}$Si$\{^{29}Si\}$ DQ spectra acquired for different dipolar recoupling times and scaled with respect to the signal intensities in the 1D $^{29}$Si MAS spectrum in (a). The experimental data in (c) are compared to calculated $^{29}$Si DQ buildup curves based on structure **1** reported in ref 33 (dotted gray lines) and structure **2** (solid red lines) found by the structure construction-and-evaluation algorithm and subsequently refined by periodic DFT lattice energy minimization. The other energy-minimized structures **3** and **4** with comparable total energies yielded similar calculated DQ buildup curves that were indistinguishable from **2**.

**Molecular Ordering in Layered Silicate Sheets.** Nevertheless, the high degree of short-range molecular order in the frameworks of surfactant-directed layered silicate materials is directly reflected in their solid-state $^{29}$Si NMR spectra. Specifically, the 1D $^{29}$Si$\{^1H\}$ CP-MAS NMR spectrum in Figure 3a (black) of the layered silicate-$C_{16}N^+Me_2Et$ material consists of five narrow (0.5−1 ppm, full-width-half-maximum, fwhm) resonances at −97.0, −101.0, −103.7, −109.1, and −114.7 ppm with similar intensities, indicating that the silicate layers are highly ordered at the molecular level and that they contain five distinct Si framework sites in the structure (labeled 1−5, respectively). Quantitative single-pulse $^{29}$Si MAS NMR measurements have established that the Si framework sites are equally populated,[33] with $^{29}$Si chemical shift tensor analyses showing that peaks 1 and 2 are associated with incompletely cross-linked $Q^3$ $^{29}$Si moieties (i.e., $(SiO)_3\textbf{Si}-O^-$ or $(SiO)_3\textbf{Si}-OH$), while peaks 3, 4, and 5 are fully cross-linked $Q^4$ $^{29}$Si sites (i.e., $\textbf{Si}(OSi)_4$).[51] Two-dimensional dipolar-mediated $^{29}$Si$\{^{29}Si\}$ correlation NMR techniques can be used to probe interconnectivities among the different Si framework sites, by using advanced radio frequency (rf) pulse sequences to reintroduce internuclear $^{29}$Si−$^{29}$Si dipole−dipole couplings. For example, a 2D DQ correlation $^{29}$Si$\{^{29}Si\}$ NMR spectrum (Figure 3b) acquired for the layered $C_{16}N^+Me_2Et$-silicate material exploits through-space $^{29}$Si−$^{29}$Si dipole−dipole couplings to identify distinct $^{29}$Si−O−$^{29}$Si framework moieties.

The term "double quantum" refers to the filter used to selectively detect pairs $(i,j)$ of signals from distinct $^{29}$Si nuclei that are in sufficiently close spatial proximities (typically up to 3−8 Å depending on experimental conditions) to exchange magnetization via $^{29}$Si−$^{29}$Si couplings. Such a DQ filter leads to correlated signal intensities in the 2D spectrum from distinct dipole−dipole-coupled $^{29}$Si−$^{29}$Si spin pairs that appear at the distinct frequencies (isotropic $^{29}$Si chemical shifts) of the respective sites in the horizontal ("direct") dimension and at the sum of both frequencies in the vertical ("indirect") double-quantum dimension, i.e., at positions $(\omega_i + \omega_j, \omega_i)$ and $(\omega_i + \omega_j, \omega_j)$. The 2D $^{29}$Si$\{^{29}Si\}$ DQ correlation NMR spectrum in Figure 3b was acquired using a short (5 ms) DQ recoupling time (corresponding to a delay during which the dipolar couplings are reintroduced), such that only $^{29}$Si−O−$^{29}$Si spin pairs in close spatial proximities (< ∼4 Å) yield correlated signal intensities. Consequently, the spectrum reveals pairs of correlated signals among the five $^{29}$Si sites that allow their respective interconnectivities (via bridging oxygen atoms) to be established within the silicate framework. These results are consistent with previous conclusions drawn from complementary $^{29}$Si$\{^{29}Si\}$ DQ correlation measurements mediated by through-bond scalar ($J$) couplings, which thus establish unambiguously the $^{29}$Si−O−$^{29}$Si connectivities in the layered silicate material, which was not possible to obtain from the scattering data.[33,51]

Importantly, dipolar couplings depend strongly $(1/r^3)$ on the distances $(r)$ separating $^{29}Si-^{29}Si$ spin pairs, which provide sensitive additional constraints on the silicate framework structure. These can be obtained by acquiring a series of 2D $^{29}Si\{^{29}Si\}$ DQ spectra at different dipolar recoupling times. The vast majority of dipolar-recoupled $^{29}Si-^{29}Si$ nuclei can be considered as isolated spin pairs due to the modest natural abundance of $^{29}Si$ (4.7%), yielding correlated 2D signals whose intensities depend on their internuclear separation distances $r$ in a relatively straightforward manner. Closer and more strongly coupled $^{29}Si-O-^{29}Si$ species exhibit more intense correlated signals, which buildup more rapidly with recoupling time compared to more distant and therefore more weakly coupled pairs of framework $^{29}Si$ sites. The dependences of the intensities of the correlated $^{29}Si$ DQ signals on the dipolar recoupling time (referred to as "DQ buildup curves") can be measured, quantitatively analyzed, and exploited to evaluate framework models based on associated sets of $^{29}Si-^{29}Si$ distances and simulated $^{29}Si$ build-up curves.[4,66] For example, Figure 3c shows $^{29}Si$ DQ buildup curves measured (black squares) that represent summed contributions for each of the distinct dipole−dipole-coupled $^{29}Si(i)-^{29}Si(j)$ spin pairs within the silicate framework. The rapid buildup of $^{29}Si\{^{29}Si\}$ DQ signal intensities observed at short (<10 ms) recoupling times for $^{29}Si-O-^{29}Si$ site pairs 2-1, 3-1, 4-2, 4-3, 5-1, 5-2, 5-3, and 5-4 manifest strong dipolar couplings that are associated with the close (<4 Å) proximities of these $^{29}Si$ sites, which are covalently linked through bridging oxygen atoms. By comparison, the slower buildup of $^{29}Si\{^{29}Si\}$ DQ intensities observed for $^{29}Si-O-^{29}Si$ site pairs 1-1, 2-2, 3-2, 3-3, 4-1, 4-4, and 5-5 manifest their weaker couplings and greater separation distances within the silicate framework. Such $^{29}Si\{^{29}Si\}$ DQ buildup curves present new and independent structural constraints that can be used to test the validity of candidate layered silicate framework structures, or fragments of such structures, as the frameworks are constructed.

Specifically, theoretical buildup curves can be generated for each of the distinct $^{29}Si(i)-^{29}Si(j)$ site pairs in different candidate structures and evaluated against the experimental $^{29}Si\{^{29}Si\}$ DQ measurements. For a given set of Si atomic coordinates and neglecting the small probability of multispin clusters,[4,66] the $^{29}Si$ DQ buildup curves associated with each pair of $^{29}Si$ sites $i$ and $j$ are calculated as sums of known individual analytical functions for $^{29}Si(i)-^{29}Si(j)$ distances shorter than a specified cutoff value (usually 8 Å).[99] Importantly, it is not possible to do the opposite and directly extract $^{29}Si-^{29}Si$ distances from the DQ build-up curves. Rather, as for structure−solution protocols based on powder diffraction data, it is necessary instead to search the conformational space to find structures (or structure fragments) that yield simulated DQ curves that are evaluated with respect to their overall agreement with the experimental data (as represented by the parameter $R_{DQ}$). Fitting the $^{29}Si$ DQ buildup curves calculated for a given structure to the experimentally measured plots requires only two parameters: a scaling factor and a parameter that describes the decay of $^{29}Si$ DQ intensities, which are assumed identical for all of the dipole−dipole-coupled $^{29}Si(i)-O-^{29}Si(j)$ spin pairs (an assumption that has proven valid for zeolites).[4,66] For example, using the framework structure previously proposed[33] for the layered silicate-$C_{16}N^+Me_2Et$, referred to as candidate structure **1**, a series of $^{29}Si$ DQ buildup curves were calculated for each distinct pair of $^{29}Si-O-^{29}Si$ sites, based on their respective

distances in the proposed structure, yielding the dashed lines in Figure 3c. They are in reasonable qualitative agreement with the experimental data, although there are several noticeable deviations. In particular, several of the calculated curves predict more gradual intensity buildup than measured experimentally (e.g., for $^{29}Si-^{29}Si$ pairs 2-1 and 4-4), while others predict more rapid buildup (e.g., $^{29}Si-^{29}Si$ pairs 1-1, 3-1, and 4-1). Most of these site pairs correspond to non-nearest-neighbor framework atoms, which indicates that while structure **1** fulfills the established connectivities and other constraints provided by previously available experimental and modeling results,[33] it does not entirely capture the longer-range arrangements of Si atoms in the unit cell. The $^{29}Si\{^{29}Si\}$ DQ NMR analyses provide important new longer-range $^{29}Si-^{29}Si$ distance constraints that allow more accurate structural representations of this challenging noncrystalline material to be established than previously possible.

**Structure Determination of Locally Ordered but Noncrystalline Frameworks.** New candidate framework structures can be constructed that are compatible with all of the $^{29}Si(i)-O-^{29}Si(j)$ site interconnectivities and distance constraints established by $^{29}Si\{^{29}Si\}$ DQ NMR. A comprehensive search for plausible silicate framework structures was conducted using a protocol similar to one developed for solving zeolite crystal structures,[66] but which had to be modified to accommodate the much lower extent of overall molecular order in the material and absence of *a priori* knowledge of the "crystallographic" space group of the framework. This significantly extends and broadens the utility of this approach to permit, for the first time, the determination by NMR of framework structures for which a space group is not known.[81]

We summarize the protocol by which framework structures can be established even for partially ordered materials that lack long-range crystallographic order. The structure construction-and-evaluation algorithm requires five principal pieces of information as inputs: (i) the unit cell parameters (e.g., $a$ = 9.10 Å, $b$ = 7.28 Å, $c$ = 33.5 Å, $\alpha = \beta = 90°$, and $\gamma = 111°$, as extracted from the PXRD data, Figure 1); (ii) the number and occupancies of distinct Si sites (e.g., the five equally populated sites as measured by quantitative 1D single-pulse $^{29}Si$ MAS NMR[51]); (iii) the number of equivalent Si sites per unit cell (two, as described in SI); (iv) the Si−O−Si interconnectivity relationships between distinct Si sites (e.g., 1-2, 1-3, 1-5, 2-4, 2-5, 3-5, 4-5, and the doubly connected 3-4 pair, as established by $^{29}Si-^{29}Si$ correlation experiments,[33] Figure 3b); and (v) distance-dependent $^{29}Si-^{29}Si$ dipolar interactions between both directly bonded and longer-range pairs of Si sites, as provided by $^{29}Si\{^{29}Si\}$ DQ buildup curves (Figure 3c).

Collectively, these inputs provide constraints that are crucial to the construction and evaluation of candidate structural models. In addition, the algorithm incorporates information derived from siliceous zeolite structures that have been solved by crystallography analyses. This includes in particular the distances between Si sites that are covalently bonded via bridging oxygen atoms, which are initially set to 3.1 Å, the average value established separately by single-crystal diffraction analyses of various zeolites.[66] With these inputs, candidate structural models for the framework can be constructed that satisfy all of the experimental constraints. Normally, a further criterion is imposed that there should be no "three-membered rings" of Si sites in the bulk framework structure, as these are energetically unfavorable and rare in silicate network materials.[100] Because known structures of layered silicates are

not nearly as numerous as they are for zeolites, the structure construction-and-evaluation algorithm and corresponding calculations were performed with and without allowances for three-membered rings. In the end, only structures with four-membered rings were found to be fully consistent with all available experimental data.

The framework construction-and-evaluation algorithm employs a sequential combinatorial approach in which candidate structures are built up one atom at a time. At each step, only the partial structures are selected that satisfy all of the criteria of relative $^{29}$Si site populations, interconnectivities, separation distances, and equivalences of local structure for Si atoms of the same site type within the unit cell. Only the group of candidate structure fragments having the highest-quality fits to the $^{29}$Si DQ intensity buildup curves are passed onto the next atom-insertion step. (At each step, only those fragments with $R_{DQ} < 1.2 \times \min(R_{DQ})$ are advanced, where $\min(R_{DQ})$ is the structure with the best quality fit to the DQ buildup curves at any particular step.) The details of how candidate structures are built up are described in ref 81. Once all atoms have been added, each candidate structure is subjected to a minimization of its atomic coordinates against a cost function that includes the overall quality of fit to the $^{29}$Si DQ buildup curves, the deviation from an expected distance (3.1 Å) separating Si atoms known to be connected, and equivalence of local structure for atoms of the same site type, which can be quantified using the approach in ref 81. The candidate frameworks within the set of minimized structures are then sorted according to their qualities of fit to the DQ buildup curves.

Using this new structure construction-and-evaluation algorithm, four candidate structures without three-membered rings were identified for the layered silicate-C$_{16}$N$^+$Me$_2$Et framework, all of which are consistent with the XRD and $^{29}$Si DQ NMR data. The four new candidate frameworks are referred to as structures 2−5 and are shown in Figure S4, along with structure 1 (from ref 33). Three additional structures containing three-membered rings (structures 6−8 in Figure S4) were also found, but in each case their respective DFT-calculated energies were significantly higher than the other candidate structures and their DFT-calculated $^{29}$Si chemical shifts were markedly different from the experimentally measured shifts. Based on these structure-validation criteria (discussed in detail below), the three-membered-ring-containing structures were rejected as candidate structures (see SI). As an example, theoretical $^{29}$Si DQ buildup curves calculated for the different pairs of $^{29}$Si-($i$)−$^{29}$Si($j$) sites in structure 2 (after energy optimization, see below) are shown as solid red lines in Figure 3c for comparison with the experimental data; all of the buildup curves in the different panels manifest improved agreement with the data, compared to structure 1. The qualities of fits to the $^{29}$Si DQ buildup curves obtained for the five candidate structures are represented by their respective $R_{DQ}$ values, which are listed in Table 1. Structures 2−5 all exhibit better agreement with the new $^{29}$Si DQ buildup curve constraints than does structure 1.

As described in ref 81, this structure construction-and-evaluation algorithm tests in a general manner for the existence of symmetry relationships between atoms of the same site-type in the unit cell (e.g., Si1, Si2, etc.) by examining whether their local environments are identical. Consequently, the space group for a given structure is identified by examining the structure *after* it has been generated by the algorithm, rather than requiring knowledge of the space group *a priori*. Each of these NMR-determined structures was found to have the Si atoms of

**Table 1. Lattice Energies and Agreement Factors between Calculated and Experimental $^{29}$Si NMR Results**[a]

| candidate structure | $E$ (eV) | $R_{DQ}$[b] (pre-DFT) | $R_{DQ}$[c] (optimized) | $\chi^2_{CS}$[d] | $\chi^2_J$[e] | $\chi^2_J$[e,f] |
|---|---|---|---|---|---|---|
| 1 | −11432.6 | 0.255 | 0.255 | 15.0 | 292 | 174 |
| 2 | −11436.0 | 0.159 | 0.171 | 4.0 | 545 | 119 |
| 3 | −11435.9 | 0.165 | 0.174 | 6.6 | 419 | 34 |
| 4 | −11435.8 | 0.167 | 0.184 | 5.0 | 577 | 55 |
| 5 | −11430.8 | 0.176 | 0.205 | 13.7 | 398 | 150 |

[a]Based on $^{29}$Si isotropic chemical shifts (Figure 3a), $^{29}$Si DQ intensity buildup curves (Figure 3c), and $^2J(^{29}$Si−O−$^{29}$Si) couplings (see below). [b]Before plane-wave-based DFT energy minimization. [c]After plane-wave-based DFT energy minimization (with fixed unit cell parameters). [d]$\chi^2_{CS} = \sum_i[\delta_{calc}(i) - \delta_{exp}(i)/\sigma_{CS,exp}(i)]^2$, where $\delta_{exp}(i)$ is the position of the $^{29}$Si MAS NMR signal measured at 298 K for site $i$ and $\sigma_{CS,exp}(i)$ the associated fwhm. $\delta_{calc}$ is calculated by a plane-wave-based DFT approach using the referencing method described in SI. [e]$\chi^2_J = \sum_i[(J_{calc}(i) - J_{exp}(i))/\sigma_{J,exp}(i)]^2$, where $J_{calc}$ was obtained from DFT calculations using cluster approaches and $\sigma_{J,exp}(i)$ is the uncertainty associated with each measured coupling constant calculated as described in the Materials and Methods Section. [f]Considering $Q^4-Q^4$ $^{29}$Si−O−$^{29}$Si site pairs 3-4(a), 3-4(b), 3-5, and 4-5 only.

the same site-type related by inversion symmetry. Although this material lacks the coherence between layers to be considered truly crystalline, the symmetry within the silicate layer can be best described by the $P\bar{1}$ space group in which the only symmetry element is an inversion center. As discussed in more detail below, all of these structures furthermore share a number of other similarities, such as the presence of Si3−Si4−Si3−Si4 four-member rings, and in some but not all cases, the numbers and types of ring structures of which the frameworks are composed (e.g., four-, five-, and six-member rings) and/or their sequences of Si sites within such rings.

**Lattice Energy Minimization of Candidate Frameworks.** The NMR-based approach used here for determining silicate framework structures begins by providing the approximate relative positions of distinct $^{29}$Si atoms within a unit cell. Additional steps are required to establish and refine realistic positions of all Si, O, and H atoms within the unit cells of candidate structures. Various methods are available to perform such structure refinements, depending on the nature of the material. For example, for materials that exist as single crystals of suitable dimensions (usually >50 $\mu$m), refinement of the structure against single-crystal XRD data, if available, provides highly accurate structures. For materials that exhibit long-range 3D atomic order but lack suitably large single crystals, appropriate structure construction algorithms combined with Rietveld refinement[101] against PXRD data can be used to determine their structures, which are generally less accurate than for single-crystal analyses. However, in the absence of long-range 3D atomic order, as is the case here and as generally associated with stacking disorder in layered materials, diffraction methods are severely limited, and Rietveld refinement of candidate structures is generally not possible. For silicates, alternative approaches have used least-squares minimizations of interatomic distances based on those known for siliceous zeolite framework structures[102] and/or using additional NMR constraints. The latter exploits the highly localized nature of NMR interactions, such as $^{29}$Si chemical shift anisotropies,[67,68] dipolar couplings,[4,66] or scalar couplings[69] each of which are sensitive in complementary ways to local bonding geometries.

Here, using all available XRD and $^{29}$Si NMR constraints, the four candidate layered silicate-C$_{16}$N$^+$Me$_2$Et frameworks identified by the structure construction-and-evaluation algorithm were refined by using DFT with periodic boundary conditions. The lattice energies provided by these DFT optimizations of the framework geometries also provide an additional criterion for assessing the various candidate structures. Full sets of starting coordinates were generated from the NMR/XRD/ algorithm-determined candidate structures by adding oxygen atoms midway between the Si atoms (known to be connected via Si−O−Si covalent bonds). In addition, −OH groups were added to $Q^3$ Si sites 1 and 2 to form approximate SiO$_4$ tetrahedra, with each H atom placed 1.0 Å from its corresponding silanol oxygen atom and with a 180° Si−O−H bond angle. To allow meaningful comparisons, framework structure **1**, which had already been relaxed in ref 33, was also reoptimized under identical conditions as used here for the other candidate structures.

The layered silicate structures obtained following lattice energy minimization of each of the candidate frameworks are shown in Figure 4, with their respective lattice energies presented in Table 1. The agreement of each optimized structure with the experimental $^{29}$Si DQ buildup curves was redetermined by recalculating the corresponding buildup curves, based on the revised Si atom positions in each optimized framework; the $R_{DQ}$ values that reflect the respective fit qualities for each of the lattice-energy-minimized structures are listed in Table 1. Notably, the $R_{DQ}$ values for optimized structures **2−4** are lower (reflecting better fits) and fall within a relatively narrow range (0.171−0.184), compared to those for structures **1** and **5**, which are significantly higher (0.205 and 0.255, respectively). Furthermore, the lattice energies associated with optimized structures **2−4** are virtually indistinguishable (within 0.2 eV from each other) and significantly lower than those obtained for optimized structures **1** and **5** (by ∼3 and 5 eV, respectively). In summary, framework structures **2−4** provide better agreement with the DQ buildup curves (smaller $R_{DQ}$ coefficients) before and after refinement and exhibit lower lattice energies than for structures **1** and **5**. These results establish that, among the large ensemble of possible framework structures that are explored and assessed by the structure construction-and-evaluation algorithm, only a small subset of three closely related structures (**2−4**) are identified as being most consistent with the experimental and modeling criteria.

**$^{29}$Si Chemical Shift Analyses of Candidate Structures.** Isotropic $^{29}$Si chemical shift interactions are sensitive to the local electron density about a given $^{29}$Si framework site, which depends strongly on local bond angles and distances. Calculations of $^{29}$Si chemical shifts from first principles and their comparisons to experimental values therefore provide means to assess the various candidate framework structures. Calculations of isotropic $^{29}$Si chemical shifts were carried out using the GIPAW approach[88,89] implemented in CASTEP[84] for each distinct $^{29}$Si site in the optimized candidate structures **1−5** for the layered silicate-C$_{16}$N$^+$Me$_2$Et framework. The results are tabulated in Table S2 and are summarized in Figure 5 as plots that correlate the calculated and experimentally measured isotropic $^{29}$Si chemical shifts. Table 1 lists the overall agreement between the experimental and calculated isotropic $^{29}$Si shifts, as quantified by a goodness-of-fit parameter, $\chi^2_{CS}$, for each candidate structure. Calculated $^{29}$Si isotropic chemical shifts for optimized structures **2−4** are in good general agreement with the experimental $^{29}$Si isotropic shifts ($\chi^2_{CS}$ values between 4
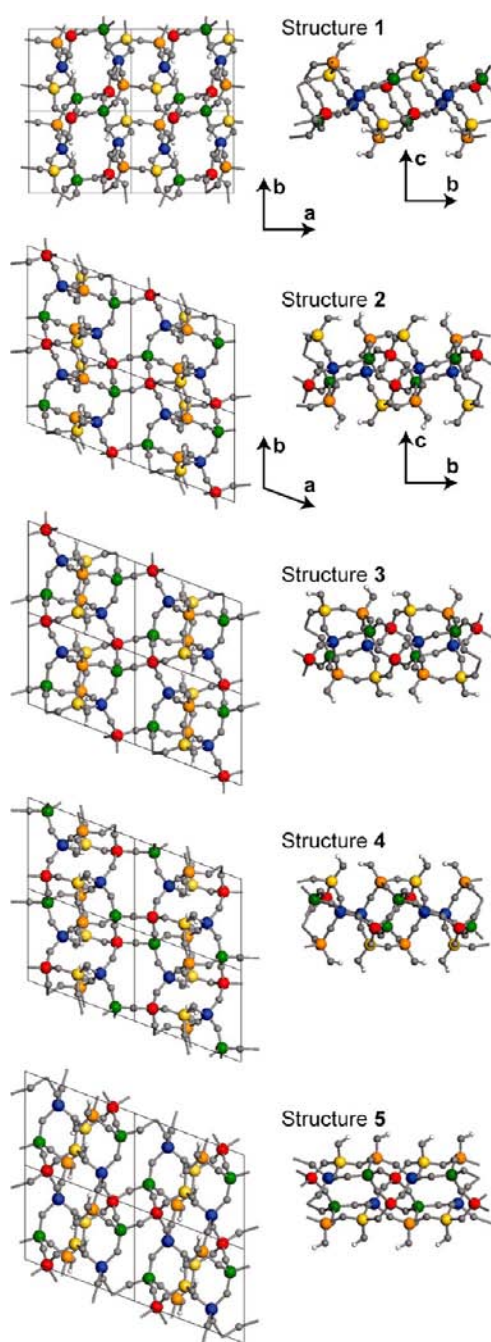


**Figure 4.** Candidate framework structures of surfactant-directed layered silicate-C$_{16}$N$^+$Me$_2$Et material with Si sites Si1−Si5 shown as yellow, orange, red, green, and blue, respectively, and O and H atoms indicated as dark and pale gray. Structure **1** was obtained after DFT optimization (using CASTEP) of the structure proposed in ref 33. Structures **2−5** are consistent with PXRD and $^{29}$Si{$^{29}$Si} DQ NMR data and obtained after DFT optimization.

and 7), whereas those calculated for structures **1** and **5** deviate significantly from the experimental values ($\chi^2_{CS}$ values >13). Similarly, the structures containing three-membered rings all led, after geometry optimization (see relaxed structures in Figure S5) to calculated $^{29}$Si chemical shift values that are in poor agreement with the experimental data ($\chi^2_{CS}$ values >16, see Table S2), consistent with the low probability of finding such structural elements in silicate materials.
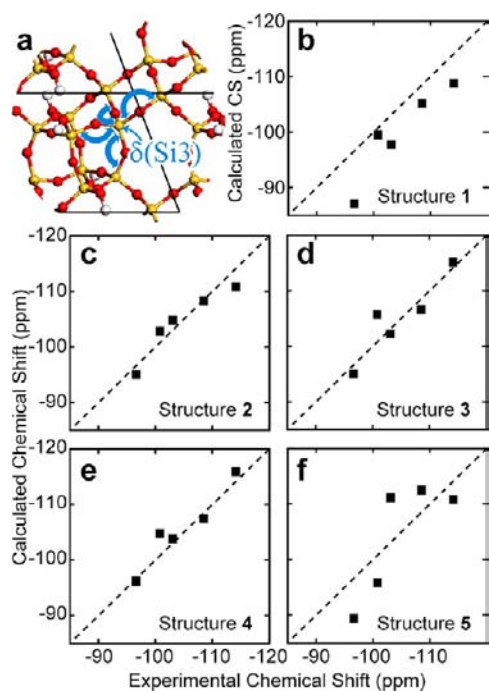
**Figure 5.** (a) Partial view (from the top) of candidate structure **3** used to conduct DFT calculations of the isotropic $^{29}$Si chemical shifts associated with Si sites in its framework, with Si, O, and H atoms shown in yellow, red, and gray, respectively. The calculated chemical shift of a given $^{29}$Si site is influenced, among other local structural features, by the Si−O−Si bond angles to all of its connected neighbors, as illustrated here for site Si3. (b−f) Comparisons of calculated and experimental isotropic $^{29}$Si chemical shifts for the DFT-refined candidate structures **1−5** of the layered silicate-C$_{16}$N$^+$Me$_2$Et framework. Correlation plots of the isotropic $^{29}$Si chemical shifts of the different $^{29}$Si sites calculated from first principles are shown versus the values measured experimentally at 298 K (the uncertainties of which are approximately the size of the symbols or smaller). In each plot, the dashed diagonal line indicates perfect agreement between experimental and calculated chemical shifts.

Previous studies[51,103] have shown that the $^{29}$Si isotropic chemical shifts associated with framework Si sites in the 1 nm-thick silicate layers are strongly influenced by interactions with the alkyl-ammonium head groups of the C$_{16}$N$^+$Me$_2$Et surfactant species and adsorbed solvent molecules at their organic−inorganic surfaces. Omitting the surfactant and solvent molecules in the DFT calculations is expected to have two effects. First, the framework geometry of minimum energy might be different in the presence or absence of the surfactant or solvent species. As discussed above, the negative charges associated with nonbridging oxygen atoms of the $Q^3$ Si moieties are compensated in the latter case by the addition of H atoms, which tend to form interactions with surrounding oxygen atoms in the course of the optimization and cause local distortions of the frameworks as a result. Second, interactions between silicate framework sites and the surfactant or solvent species across their large common surface area are expected to induce perturbations of the electronic density at $^{29}$Si sites within the silicate framework that could affect their $^{29}$Si isotropic chemical shifts.[103] These effects are probably of the order of the small differences observed among the $^{29}$Si chemical shifts calculated from structures **2−4**, making it difficult to differentiate among these structures on the basis of their respective isotropic $^{29}$Si chemical shifts. Nevertheless, as for the total lattice energies

and the agreement with the DQ buildup curves, structures **2−4** again yield closely comparable results that agree significantly better with the experimental data than do structures **1** and **5**. Thus, while structures **1** and **5** would have been difficult to eliminate unambiguously on the sole basis of their agreement with the experimental $^{29}$Si DQ NMR data, the additional calculated lattice energies and $^{29}$Si chemical-shift constraints provided by the DFT calculations all concur to indicate that structures **2−4** are more valid structural models.

**Measurements and Calculations of $^2J(^{29}$Si−O−$^{29}$Si) Couplings.** Through-bond scalar ($J$) couplings between pairs of $^{29}$Si nuclei in $^{29}$Si−O−$^{29}$Si framework moieties offer new opportunities to generate additional independent constraints to further establish the validity of and potentially distinguish between the candidate structural models. Scalar couplings are sensitive to the local bonding environments of covalently linked atoms and have recently been emerging as quantitative new means to probe the molecular structures of solids.[69,70,80,104−106] In silicates, $^2J(^{29}$Si−O−$^{29}$Si) couplings directly manifest the existence of covalent bonds (via oxygen atoms) between $^{29}$Si sites in the framework and are expected to reflect mainly their local bond distances and angles, in particular the $^{29}$Si−O−$^{29}$Si bond angle.[69,70] The sensitivity of $^2J(^{29}$Si−O−$^{29}$Si) couplings to their local bonding environments has been demonstrated in recent studies of siliceous zeolite materials,[69] which showed that such couplings could be predicted by DFT calculations of small atomic clusters extracted from the framework structure. Scalar $^2J(^{29}$Si−O−$^{29}$Si) couplings are thus expected to provide additional structural constraints to complement those discussed above.

Consequently, we hypothesized that differences in the respective scalar $^2J(^{29}$Si−O−$^{29}$Si) couplings predicted by DFT calculations for the various candidate structures **1−5** could be used to differentiate among them, based on comparisons with experimentally measured values. Measurements of such scalar couplings were conducted on a partially (50%) $^{29}$Si-enriched[107] layered silicate-C$_{16}$N$^+$Me$_2$Et material that was otherwise identical to that used in Figures 1−5. Figure 6a,b shows a 1D $^{29}$Si{$^1$H} CP-MAS NMR spectrum of this material, along with a typical spin−echo modulation plot (blue uncertainty bars) for a pair of $J$-coupled spins, in this case for $^{29}$Si framework sites Si1 and Si5, as separately measured by using the $z$-filtered IPAP rf-pulse sequence shown in Figure S6. The frequency of the oscillations of the $^{29}$Si NMR signal intensity, as a function of the half-spin−echo duration $\tau$, is directly proportional to the magnitude of the scalar coupling for this specific site pair. The modulated $^{29}$Si signal intensity was obtained by using frequency-selective rf pulses to manipulate independently the NMR signals associated with $^{29}$Si sites Si1 (at −96.6 ppm) and Si5 (at −114.1 pm) and is thus due specifically to the $^2J(^{29}$Si−O−$^{29}$Si) coupling between sites Si1 and Si5. The coupling value can be extracted by fitting the spin−echo intensities to a function[107] (e.g., red curve, Figure 6b) that accounts for the presence of a nonmodulated signal component due to partial enrichment (see equation S2). Simulations described in Figure S8 establish that these measurements are particularly robust with respect to possible deviations from the magic angle, which can reintroduce residual homonuclear dipolar couplings,[108,109] but which are shown to have a negligible effect on the analyses here. As shown in Table 2, $^2J(^{29}$Si−O−$^{29}$Si) couplings were thus obtained for all covalently bonded $^{29}$Si−O−$^{29}$Si pairs of sites in the 50% $^{29}$Si-enriched framework of the C$_{16}$N$^+$Me$_2$Et-silicate material, including for the doubly coupled pair Si3−Si4
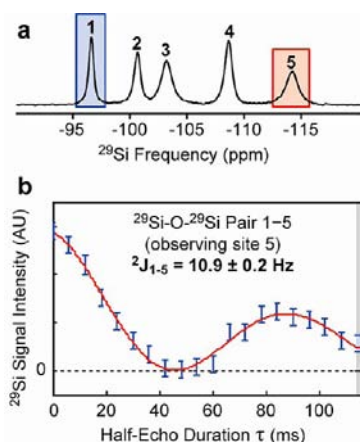
**Figure 6.** (a) 1D $^{29}Si\{^1H\}$ CP-MAS NMR spectrum of a layered silicate-$C_{16}N^+Me_2Et$ material prepared with 50% isotopic enrichment in $^{29}Si$. (b) Representative modulation of the $^{29}Si$ signal associated with site 5 (highlighted in red in (a)) due to its $^2J(^{29}Si-O-^{29}Si)$ coupling to site 1 (highlighted in blue in (a)), measured by using the z-filtered IPAP experiment (see Figure S6) with frequency-selective rf pulses. The error bars reflect the estimated uncertainties associated with measurements of the signal intensities of $^{29}Si$ site 5 for the different half-spin−echo delays $\tau$. By fitting the data points (blue) to a function (red curve) that accounts for the effects of J-coupling interactions and coherence dephasing, the corresponding $^2J(^{29}Si-O-^{29}Si)$ coupling between sites 1 and 5 is determined to be $10.9 \pm 0.2$ Hz (see equations S2 and S3).

**Table 2. $^2J(^{29}Si-O-^{29}Si)$ Couplings Measured for the Layered $C_{16}N^+Me_2Et$-Silicate with 50% $^{29}Si$ Enrichment[a]**

| $^{29}Si(i)-O-^{29}Si(j)$ site pair | $J$ (Hz) |
|---|---|
| 1-2 | $8.6 \pm 0.2$ |
| 1-3 | $5.3 \pm 0.3$ |
| 1-5 | $10.9 \pm 0.2$ |
| 2-4 | $10.8 \pm 0.1$ |
| 2-5 | $12.3 \pm 0.2$ |
| 3-4(a)[b] | $9.2 \pm 0.5$ |
| 3-4(b)[b] | $11.7 \pm 0.5$ |
| 3-5 | $11.1 \pm 0.2$ |
| 4-5 | $15.2 \pm 0.2$ |

[a]See Figures S6 and S7. [b]See SI for doubly coupled $^{29}Si-O-^{29}Si$ spin pair 3-4. The $J_{3-4(a)}$ and $J_{3-4(b)}$ labels were chosen such that $J_{3-4(a)} \leq J_{3-4(b)}$.

(Figure S7). The estimated accuracy of the measured couplings ($< \pm 0.5$ Hz for all spin pairs) is significantly greater than previously achieved for similar materials.[78] Such high measurement accuracies, even for weakly J-coupled $^{29}Si-O-^{29}Si$ spin pairs (<10 Hz), took advantage of the relatively high mobilities of the adsorbed surfactant species in these materials at room temperature, which allowed relatively low MAS spinning speeds and moderate rf decoupling powers to be used. Such conditions are expected to be useful generally in similar investigations of other hybrid molecular systems.

The $^2J(^{29}Si-O-^{29}Si)$ couplings thus measured provide new experimental constraints for discriminating between the candidate layered-silicate structures, in combination with the diffraction, solid-state $^{29}Si$ NMR, and modeling analyses. DFT calculations of $^2J(^{29}Si-O-^{29}Si)$ couplings were subsequently conducted using cluster approaches, whose accuracy was recently demonstrated for crystalline siliceous zeolites[69] and crystalline and glassy calcium silicates.[70] Specifically, small O-
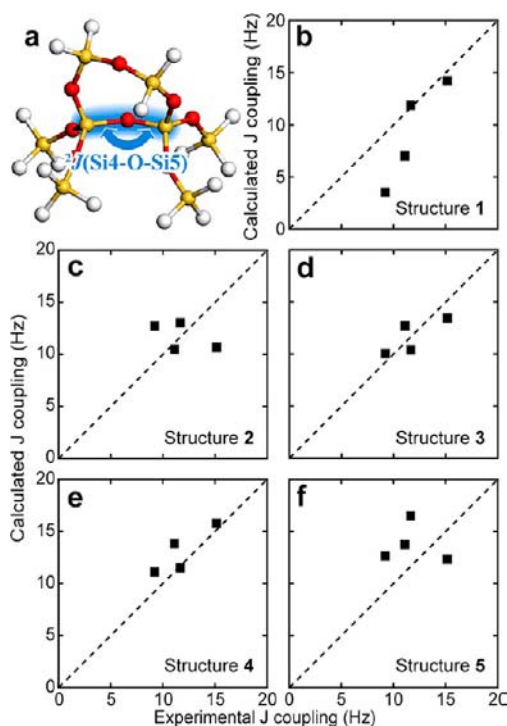


**Figure 7.** (a) A representative cluster used for the DFT calculations of J couplings (here, for the $^{29}Si-O-^{29}Si$ site pair 4-5 in structure **4**) with Si, O, and H atoms shown in yellow, red, and white, respectively. The $^2J(^{29}Si-O-^{29}Si)$ coupling associated with a given pair of covalently connected $^{29}Si$ sites is primarily influenced by the associated Si−O−Si bond angle. (b−f) Comparisons of calculated and experimental $^2J(^{29}Si-O-^{29}Si)$ couplings for the various DFT-refined candidate structures of the layered silicate-$C_{16}N^+Me_2Et$ framework. Only couplings between $Q^4-Q^4$ $^{29}Si-O-^{29}Si$ pairs are shown here, for which the analyses are expected to be most reliable. Uncertainties of the experimental values are smaller than the symbols. In each plot, the dashed diagonal line indicates perfect agreement between the experimental and calculated J couplings.

centered SiH-terminated clusters, an example of which is shown in Figure 7a, were extracted for each individual pair of interconnected $^{29}Si-O-^{29}Si$ sites in each of the candidate layered silicate structures **1−5** described above (see Experimental section). Systematic calculations of $^2J(^{29}Si-O-^{29}Si)$ couplings were conducted, the results of which are reported in Table S4. It is noteworthy that all of the calculated J couplings are positive, which suggests that the true J couplings in the material are also likely positive; the experimental measurements yield only absolute values. The calculated couplings are largely dominated by the Fermi contact term,[110] with other contributions accounting for <1 Hz in all of the cases examined. Table 1 (penultimate column) summarizes the overall agreements between the respective experimental and calculated $^2J(^{29}Si-O-^{29}Si)$ couplings, as represented by a goodness-of-fit parameter $\chi_J^2$ for each site pair in candidate structures **1−5**.

In particular, important observations can be made by focusing on the results of DFT calculations for the $^2J(^{29}Si-O-^{29}Si)$ couplings involving the $Q^4$ $^{29}Si$ sites in the $C_{16}N^+Me_2Et$-silicate framework, for which confidence is expected to be high.[111] Figure 7b−f shows comparisons between the calculated and experimentally measured $^2J(^{29}Si-O-^{29}Si)$ couplings for the $Q^4-Q^4$ $^{29}Si-O-^{29}Si$ pairs 3-4(a), 3-4(b), 3-5, and 4-5 in the five candidate structures. The $\chi_J^2$ values

5650

dx.doi.org/10.1021/ja311649m | J. Am. Chem. Soc. 2013, 135, 5641−5655

that result from considering these $Q^4$–$Q^4$ $^{29}$Si–O–$^{29}$Si pairs are listed in the last column of Table 1. Interestingly, the three candidate structures **2**–**4** that were consistently validated above are also the ones that yield better agreement between the calculated and experimental $^2J(^{29}$Si–O–$^{29}$Si) couplings: goodness-of-fit values $\chi_J^2$ of 119, 34, and 55 were obtained for structures **2**–**4**, respectively, compared to 150 and 174 for structures **1** and **5**). This adds to the confidence that structures **2**–**4** are the more accurate representations of the framework structure(s) in the layered silicate-$C_{16}N^+Me_2Et$ material examined here.

It is noteworthy that, while structures **2**–**4** are very difficult to distinguish based on all other constraints used previously, there appears to be noticeable differences among their $^2J(^{29}$Si–O–$^{29}$Si) couplings. Such differences may be attributed, in particular, to differences in the $^{29}$Si–O–$^{29}$Si bond angles that are present in the different structures. This is because, unlike isotropic $^{29}$Si chemical shifts or $^{29}$Si–$^{29}$Si dipolar couplings, each $^2J(^{29}$Si–O–$^{29}$Si) coupling is mostly affected by the corresponding (single) $^{29}$Si–O–$^{29}$Si bond angle between the covalently bonded sites and to lesser (though non-negligible) extents by other parameters, such as dihedral angles.[69] By comparison, isotropic $^{29}$Si chemical shifts are affected to similar degrees by three or four different Si–O–Si bond angles that connect each framework $^{29}$Si atom to its nearest neighbors. Similarly, $^{29}$Si–$^{29}$Si dipolar couplings are not measured individually but derived from sums of individual pairwise contributions over various $^{29}$Si–$^{29}$Si distances (within 8 Å). Such complicated and overlapping influences may obscure, or render ambiguous, subtle distinctions among the different structures, whereas the role of a given $^{29}$Si–O–$^{29}$Si bond angle on individual $^2J(^{29}$Si–O–$^{29}$Si) couplings is much better defined and accordingly clearer to establish.

**Comparisons of Candidate Framework Structures.** Close examination of the candidate silicate-$C_{16}N^+Me_2Et$ structures allows several important observations to be made about the relationships and similarities among them. One way to compare the structures is to analyze the topologies of the silicate layers, as is often done for the characterization of new zeolite structures. The program TOTOPOL[112] provides topological information, such as coordination sequences, circuit symbols, and vertex symbols (see definitions in SI, section 6).[113] Comparisons can also be made visually by rotating and translating the various candidate structures, so their Si atoms are overlain. For example, Figure 8a shows the comparison of structure **3** (a good candidate, based on the $^{29}$Si NMR, XRD and DFT analyses) and structure **5** (which is not, based on similar criteria). While both structures share similar alternating four- and six-ring motifs involving silicon atom sites Si3–Si5, there are noticeable differences in their positions and their respective connectivities to sites Si1 and Si2. This and a number of other differences between structure **5** and structures **2**, **3**, or **4** are confirmed by topological analyses (see Table S5), which demonstrate that the latter are topologically distinct from structure **5** (and also structure **1**).

By comparison, topological analyses of structures **3** and **4** reveal that their corresponding Si sites have identical topological characteristics in both structures (Table S5). Figure 8b shows that when structures **3** and **4** are overlain, the frameworks are essentially identical, with only small differences in the Si atom positions and different orientations for the silanol groups associated with the incompletely condensed $Q^3$ sites Si1 and Si2.[114] Such close structural similarities are notably
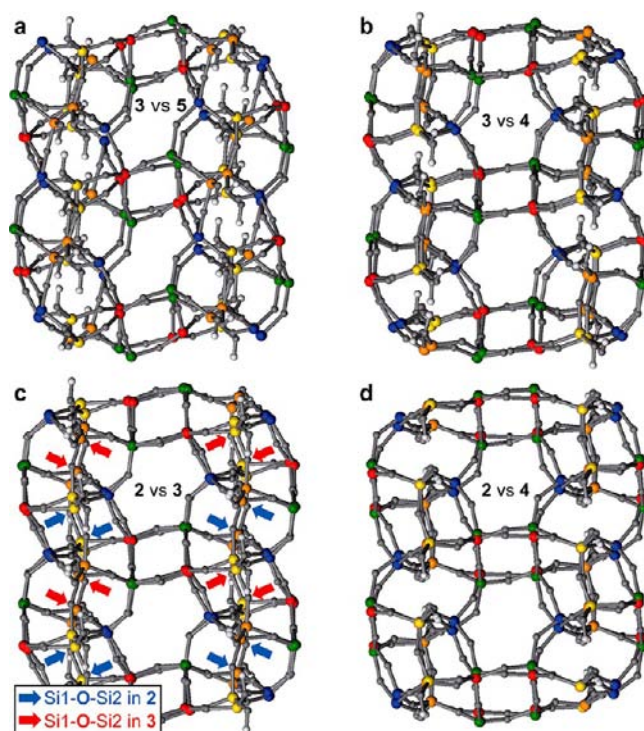


**Figure 8.** Superpositions of layered silicate-$C_{16}N^+Me_2Et$ framework structures (a) **3** and **5**, (b) **3** and **4**, (c) **2** and **3**, and (d) **2** and **4**. Si sites 1–5 are shown as yellow, orange, red, green, and blue, respectively, and O, and H atoms are indicated as gray and white. In (d), structures **2** and **4** are shown to be topologically equivalent, other than the interchange of the Si1↔Si2 and Si3↔Si4 site pairs. Blue and red arrows in (c) point to the bridging O atoms involved in the Si1–O–Si2 connectivities in structures **2** and **3**, respectively, to illustrate the distinct locations of these connectivities in these otherwise very similar frameworks.

manifested by the close agreements between their calculated and experimental $^2J(^{29}$Si–O–$^{29}$Si) couplings ($\chi_J^2$ values of 34 and 55 for structures **3** and **4**, respectively), which are far better than for the others, including structure **2** ($\chi_J^2$ = 119). Similarly, analysis of structure **2** indicates that it shares many topological features with structures **3** and **4**, though differs by the fact that pairs of sites Si1↔Si2 and Si3↔Si4 are interchanged from the latter two. This is illustrated in Figure 8c, which shows the highly similar overlap between the Si atoms of structures **2** and **3** in most parts of their frameworks. These structures nevertheless differ in the regions corresponding to the Si1–O–Si2 connectivities, whose associated bridging O atoms are indicated by blue arrows for structure **2** and red arrows for structure **3**, showing that these connectivities are located on opposite sides of the central Si3–Si4–Si3–Si4 four-member ring in the two frameworks. Similarly, structures **2** and **4** are overlain in Figure 8d such that the positions of sites Si1 and S3 in structure **2** match with the positions of sites Si2 and Si4 in structure **4** (and vice versa). Interchanging these pairs of $Q^3$ and four-member-ring $Q^4$ Si sites still satisfies all of the $^{29}$Si chemical shift, site-interconnectivity, and distance constraints provided by 2D $^{29}$Si{$^{29}$Si} DQ NMR (Figure 3).[115] Structures **2** and **4** are thus also highly similar (including connectivities between $Q^3$ sites Si1 and Si2), though with several differences in their local bonding geometries, notably the positions of some of their bridging oxygen atoms. Because the $^2J(^{29}$Si–O–$^{29}$Si) couplings are particularly sensitive to individual $^{29}$Si–O–$^{29}$Si

bond angles, the higher $\chi_J^2$ value calculated for structure **2**, compared to structures **3** and **4**, indicates that the local geometry of structure **2** is less representative of the real silicate framework. Thus, based on all of the experimental and modeling constraints available, topologically equivalent structures **3** and **4** appear to be better model(s) of the layered $C_{16}N^+Me_2Et$-silicate framework, with closely related structure **2** also a (somewhat less likely) possibility.

Realistically, structures **2**−**4** can all be considered reasonable representations of the layered silicate-$C_{16}N^+Me_2Et$ framework, within the accuracy limits achievable for such a complicated material. Superimpositions of these structures shown in Figure 9 (in yellow, red, and dark brown for structures **2**−**4**
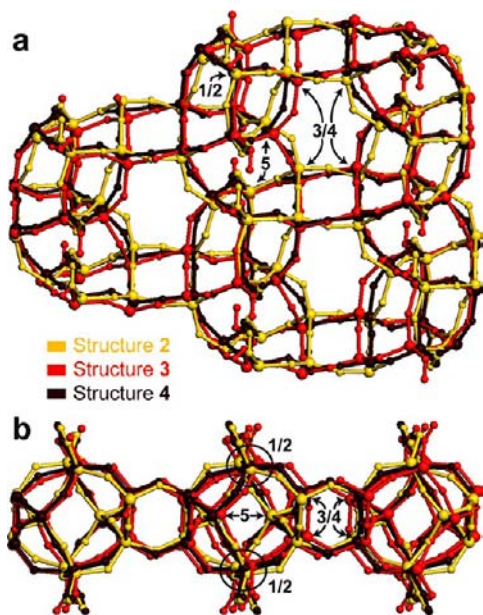


**Figure 9.** Superpositions of the three best candidate structures **2** (yellow), **3** (red), and **4** (brown) that most closely fit all of the experimental constraints: viewed (a) from the top and (b) from the side. Structures **3** and **4** appear to be the best representations of the silicate framework, within the accuracy limits of available constraints and of the modeling.

respectively) confirm that they share common longer-range features of the framework, but exhibit subtle localized differences that are distinguishable by their $^2J(^{29}Si–O–^{29}Si)$ couplings. One hypothesis is that structures **2**−**4** may all be present in the sample, either as discrete regions or as continuous distributions of atom positions among them. However, this possibility appears to be unlikely, as separate evidence suggests that candidate structures **3** and **4**, and to a lesser extent structure **2**, are all equally valid representations of a single framework structure, within the resolution limits of the analysis.

Previous studies[103] have shown that a modest extent of structural disorder is indeed present in these systems at room temperature, as revealed by modest broadening of the five resolved $^{29}Si$ signals (0.6−1.3 ppm, fwhm, compared to 0.1−0.3 ppm, fwhm, for highly crystalline siliceous zeolites).[65,116] However, rather than being due to a distribution of framework structures, such disorder was established to be associated with the local dynamics of the surfactant head groups at room temperature, which were incompletely averaged on the time scale of $^{29}Si$ NMR measurements (~$10^{-6}$ s). A distribution of

local headgroup interactions results in a distribution of local valence-electron environments for otherwise identical lattice-ordered framework $^{29}Si$ sites (in analogy to what has been recently established for $^{77}Se$ sites in semiconducting nanocrystals).[117] At temperatures substantially below 0 °C, this leads to significant broadening of the $^{29}Si$ MAS NMR signals (2.5−4.2 ppm, fwhm, at −80 °C). Such broadening is averaged out at moderate temperatures (e.g., 60 °C), where surfactant headgroup motions become fast relative to the $^{29}Si$ NMR time scale, leading to five sharp and well resolved $^{29}Si$ signals (0.4−1.0 ppm, fwhm) for the still relatively rigid Si framework sites.[103] This is consistent with the presence of a single $C_{16}N^+Me_2Et$-silicate framework structure, as opposed to several discrete structures or a continuous distribution.

The "true" structure of the layered silicate-$C_{16}N^+Me_2Et$ framework is expected to be very close to topologically identical structures **3** and **4**, further refinements of which are limited by intrinsic and subtle surface interactions and dynamics that currently are challenging to model. In particular, the temperature-dependent influences of surfactant dynamics on local silicate environments (discussed above) result in nonlinear variations of the $^{29}Si$ isotropic chemical shifts that complicate modeling analyses.[103] By comparison for organic crystals, agreement between experimental and calculated $^1H$ and $^{13}C$ chemical shifts for −OH groups can be substantially improved by linearly extrapolating the measured shifts from near-ambient temperature to 0 K (the relevant temperature for the DFT calculations).[24,118] The nonlinear temperature-dependences of the experimental $^{29}Si$ chemical shifts associated with the layered silicates, however, render such an approach impractical here. Furthermore, some siliceous zeolites[119] and layered silicates[120] are known to undergo significant temperature-dependent changes in their intrinsic framework structures (i.e., space group). Such changes can have dramatic effects on the corresponding $^{29}Si$ NMR spectra of the materials (including, doubling of the number of $^{29}Si$ signals) that cannot be taken into account by a simple linear extrapolation with temperature. Finally, more detailed molecular descriptions of the surfactant head groups, over the use of far simpler -SiOH groups (which appear relatively insensitive to temperature), would yield more realistic models of their interactions with the silicate frameworks. Nevertheless, the combined experimental and modeling analyses presented here capture the essential physical features of the layered silicate framework, whose high (but imperfect) degree of local order can be established to an extent not previously possible.

## ■ CONCLUSIONS

A new and general protocol has been developed and demonstrated for determining the framework structure(s) of materials with short-range molecular order but lacking long-range 3D crystallinity. This is possible even for structures with complicated distributions of local order and disorder through the use of new quantitative constraints on local bonding geometries provided by solid-state NMR spectroscopy and computational chemistry, in combination with (limited) XRD data. As demonstrated for the framework of a molecularly ordered silicate-surfactant hybrid material, the analysis protocol relies on a comprehensive search and identification of candidate structural models. These must be consistent with the numbers and interconnectivities of distinct framework silicon atom sites and their respective $^{29}Si–^{29}Si$ distance constraints, as obtained from 1D and 2D solid-state $^{29}Si$ NMR, along with general unit

cell geometry and dimensions provided by XRD. Practically, as the number of inequivalent Si sites increases, resolution of their distinct $^{29}Si$ signals becomes more challenging and is expected to be a primary limitation of this approach. A key feature is that candidate structures can be found without *a priori* knowledge of a crystallographic space group, which for the layered silicate considered here, could not be obtained from the diffraction data due to the intrinsic lack of 3D crystallinity of this material. A small set of candidate structures was identified as being consistent with all of the available experimental data and was subsequently refined using first-principles calculations of their total framework energies. Further evaluations of the structures were undertaken based on comparisons between isotropic $^{29}Si$ chemical shifts and $^2J(^{29}Si-O-^{29}Si)$ coupling interactions measured experimentally and calculated by DFT for each of their respective $^{29}Si$ sites. This led to three closely related candidate structures with nearly identical lattice energies and similar levels of agreement among all calculated and experimental NMR parameters.

Based on comparisons of calculated and experimental and $^2J(^{29}Si-O-^{29}Si)$ couplings, two topologically identical structures are determined to be the best representation(s) of the layered $C_{16}N^+Me_2Et$-silicate framework. The accuracies of such structures are thought to be limited predominantly by subtle dynamics of the surfactant species and their interactions with the inorganic framework in the complicated nanocomposite material itself, which lead to uncertainties in the DFT calculations. More advanced modeling treatments that account for the effects of the structure-directing surfactant and/or solvent species on $^2J(^{29}Si-O-^{29}Si)$ couplings and isotropic $^{29}Si$ chemical shifts can be expected to lead to improved quantitative analyses of these and related framework structures. The use of $^2J(^{29}Si-O-^{29}Si)$ couplings and their calculations in extended systems,[121] in particular, provides important new means and opportunities to distinguish and/or refine structures that are otherwise similar in their overall lattice energies, scattering data, $^{29}Si-^{29}Si$ distances, and $^{29}Si$ environments. The approach and protocol reported here are expected to be generally applicable to other types of semi- or nanocrystalline materials, including layered silicates, zeolites, polymers, and other highly defected solids, with poor or complicated molecular order that influences their macroscopic properties.

## ASSOCIATED CONTENT

### Ⓢ Supporting Information

Additional information for solid-state NMR experiments. PXRD pattern (Figure S1), $^{29}Si$ NMR spectrum (Figure S2), and calculated reflection positions as functions of unit cell parameters (Figure S3) for an ammonium-exchanged layered silicate. Estimation of silicate layer thickness from TEM. Definition of the quality of fit to DQ curves. Candidate layered silicate structures before DFT optimization (Figure S4). Three-membered ring-containing candidate structures after DFT-optimizations (Figure S5). $^{29}Si$ chemical shifts calculated using CASTEP (Tables S1 and S2). Measurements of $^2J(^{29}Si-O-^{29}Si)$ couplings (Figures S6–S8, Table S3). First-principles calculations of $^2J(^{29}Si-O-^{29}Si)$ couplings (Table S4). Topological analyses of candidate structures (Table S5). Atomic coordinates of candidate silicate framework structures. This material is available free of charge via the Internet at http://pubs.acs.org.

## AUTHOR INFORMATION

### Corresponding Author
bradc@engineering.ucsb.edu; sylvian.cadars@cnrs-orleans.fr

### Notes
The authors declare no competing financial interest.

## REFERENCES

(1) Baerlocher, C.; Xie, D.; McCusker, L. B.; Hwang, S. J.; Chan, I. Y.; Ong, K.; Burton, A. W.; Zones, S. I. *Nat. Mater.* **2008**, *7*, 631.

(2) Moliner, M.; Willhammar, T.; Wan, W.; González, J.; Rey, F.; Jorda, J. L.; Zou, X.; Corma, A. *J. Am. Chem. Soc.* **2012**, *134*, 6473.

(3) Willhammar, T.; Sun, J.; Wan, W.; Oleynikov, P.; Zhang, D.; Zou, X.; Moliner, M.; Gonzalez, J.; Martínez, C.; Rey, F.; Corma, A. *Nat. Chem.* **2012**, *4*, 188.

(4) Brouwer, D. H.; Kristiansen, P. E.; Fyfe, C. A.; Levitt, M. H. *J. Am. Chem. Soc.* **2005**, *127*, 542.

(5) Zhang, J. X.; Pilette, M. A.; Cuevas, F.; Charpentier, T.; Mauri, F.; Latroche, M. *J. Phys. Chem. C* **2009**, *113*, 21242.

(6) Lister, S. E.; Soleilhavoup, A.; Withers, R. L.; Hodgkinson, P.; Evans, J. S. O. *Inorg. Chem.* **2010**, *49*, 2290.

(7) Johnston, K. E.; Tang, C. C.; Parker, J. E.; Knight, K. S.; Lightfoot, P.; Ashbrook, S. E. *J. Am. Chem. Soc.* **2010**, *132*, 8732.

(8) Martineau, C.; Fayon, F.; Suchomel, M. R.; Allix, M.; Massiot, D.; Taulelle, F. *Inorg. Chem.* **2011**, *50*, 2644.

(9) Martineau, C.; Mellot-Draznieks, C.; Taulelle, F. *Phys. Chem. Chem. Phys.* **2011**, *13*, 18078.

(10) Rollet, A.-L.; Allix, M.; Veron, E.; Deschamps, M.; Montouillout, V.; Suchomel, M. R.; Suard, E.; Barre, M.; Ocaña, M.; Sadoc, A.; Boucher, F.; Bessada, C.; Massiot, D.; Fayon, F. *Inorg. Chem.* **2012**, *51*, 2272.

(11) Pardal, X.; Brunet, F.; Charpentier, T.; Pochard, I.; Nonat, A. *Inorg. Chem.* **2012**, *51*, 1827.

(12) Laurencin, D.; Gervais, C.; Stork, H.; Kramer, S.; Massiot, D.; Fayon, F. *J. Phys. Chem. C* **2012**, *116*, 19984.

(13) Davies, E.; Duer, M. J.; Ashbrook, S. E.; Griffin, J. M. *J. Am. Chem. Soc.* **2012**, *134*, 12508.

(14) Véron, E.; Garaga, M. N.; Pelloquin, D.; Cadars, S.; Suchomel, M.; Suard, E.; Massiot, D.; Montouillout, V.; Matzen, G.; Allix, M. *Inorg. Chem.* **2013**, DOI: doi:10.1021/ic302114t.

(15) Brown, S. P.; Spiess, H. W. *Chem. Rev.* **2001**, *101*, 4125.

(16) Goward, G. R.; Sebastiani, D.; Schnell, I.; Spiess, H. W.; Kim, H. D.; Ishida, H. *J. Am. Chem. Soc.* **2003**, *125*, 5792.

(17) Rapp, A.; Schnell, I.; Sebastiani, D.; Brown, S. P.; Percec, V.; Spiess, H. W. *J. Am. Chem. Soc.* **2003**, *125*, 13284.

(18) Elena, B.; Emsley, L. *J. Am. Chem. Soc.* **2005**, *127*, 9140.

(19) Harris, R. K. *Analyst* **2006**, *131*, 351.

(20) Harris, R. K.; Joyce, S. A.; Pickard, C. J.; Cadars, S.; Emsley, L. *Phys. Chem. Chem. Phys.* **2006**, *8*, 137.

(21) Elena, B.; Pintacuda, G.; Mifsud, N.; Emsley, L. *J. Am. Chem. Soc.* **2006**, *128*, 9555.

(22) Mifsud, N.; Elena, B.; Pickard, C. J.; Lesage, A.; Emsley, L. *Phys. Chem. Chem. Phys.* **2006**, *8*, 3418.

(23) Harris, R. K. *J. Pharm. Pharmacol.* **2007**, *59*, 225.

(24) Pickard, C. J.; Salager, E.; Pintacuda, G.; Elena, B.; Emsley, L. *J. Am. Chem. Soc.* **2007**, *129*, 8932.

(25) Harris, R. K.; Cadars, S.; Emsley, L.; Yates, J. R.; Pickard, C. J.; Jetti, R. K. R.; Griesser, U. J. *Phys. Chem. Chem. Phys.* **2007**, *9*, 360.

(26) Salager, E.; Stein, R. S.; Pickard, C. J.; Elena, B.; Emsley, L. *Phys. Chem. Chem. Phys.* **2009**, *11*, 2610.

(27) Salager, E.; Day, G. M.; Stein, R. S.; Pickard, C. J.; Elena, B.; Emsley, L. *J. Am. Chem. Soc.* **2010**, *132*, 2564.

(28) Lai, J. F.; Niks, D.; Wang, Y. C.; Domratcheva, T.; Barends, T. R. M.; Schwarz, F.; Olsen, R. A.; Elliott, D. W.; Fatmi, M. Q.; Chang, C. E. A.; Schlichting, I.; Dunn, M. F.; Mueller, L. J. *J. Am. Chem. Soc.* **2011**, *133*, 4.

(29) Fyfe, C. A.; Brouwer, D. H.; Tekely, P. *J. Phys. Chem. A* **2005**, *109*, 6187.

(30) Fyfe, C. A.; Diaz, A. C.; Grondey, H.; Lewis, A. R.; Forster, H. *J. Am. Chem. Soc.* **2005**, *127*, 7543.

(31) Fyfe, C. A.; Brouwer, D. H. *J. Am. Chem. Soc.* **2006**, *128*, 11860.

(32) Fyfe, C. A.; Brouwer, D. H. *Can. J. Chem.* **2006**, *84*, 345.

(33) Hedin, N.; Graf, R.; Christiansen, S. C.; Gervais, C.; Hayward, R. C.; Eckert, J.; Chmelka, B. F. *J. Am. Chem. Soc.* **2004**, *126*, 9425.

(34) Folliet, N.; Roiland, C.; Bégu, S.; Aubert, A.; Mineva, T.; Goursot, A.; Selvaraj, K.; Duma, L.; Tielens, F.; Mauri, F.; Laurent, G.; Bonhomme, C.; Gervais, C.; Babonneau, F.; Azaïs, T. *J. Am. Chem. Soc.* **2011**, *133*, 16815.

(35) Bonhomme, C.; Gervais, C.; Babonneau, F.; Coelho, C.; Pourpoint, F.; Azais, T.; Ashbrook, S. E.; Griffin, J. M.; Yates, J. R.; Mauri, F.; Pickard, C. J. *Chem. Rev.* **2012**, *112*, 5733.

(36) Castellani, F.; van Rossum, B.; Diehl, A.; Schubert, M.; Rehbein, K.; Oschkinat, H. *Nature* **2002**, *420*, 98.

(37) Charpentier, T.; Ispas, S.; Profeta, M.; Mauri, F.; Pickard, C. J. *J. Phys. Chem. B* **2004**, *108*, 4147.

(38) Ferlat, G.; Charpentier, T.; Seitsonen, A. P.; Takada, A.; Lazzeri, M.; Cormier, L.; Calas, G.; Mauri, F. *Phys. Rev. Lett.* **2008**, *101*, 065504.

(39) Tielens, F.; Gervais, C.; Lambert, J. F.; Mauri, F.; Costa, D. *Chem. Mater.* **2008**, *20*, 3336.

(40) Harris, R. K. *Solid State Sci.* **2004**, *6*, 1025.

(41) Harris, R. K.; Hodgkinson, P.; Pickard, C. J.; Yates, J. R.; Zorin, V. *Magn. Reson. Chem.* **2007**, *45*, S174.

(42) *NMR Crystallography*; Harris, R. K., Wasylishen, R. E., Duer, M. J., Eds.; Wiley: New York, 2009.

(43) Charpentier, T. *Solid State Nucl. Mag.* **2011**, *40*, 1.

(44) Corma, A. *J. Catal.* **2003**, *216*, 298.

(45) Bermejo-Deval, R.; Assary, R. S.; Nikolla, E.; Moliner, M.; Roman-Leshkov, Y.; Hwang, S. J.; Palsdottir, A.; Silverman, D.; Lobo, R. F.; Curtiss, L. A.; Davis, M. E. *Proc. Natl. Acad. Sci. U.S.A.* **2012**, *109*, 9727.

(46) Jae, J.; Tompsett, G. A.; Foster, A. J.; Hammond, K. D.; Auerbach, S. M.; Lobo, R. F.; Huber, G. W. *J. Catal.* **2011**, *279*, 257.

(47) Liu, F.; Willhammar, T.; Wang, L.; Zhu, L.; Sun, Q.; Meng, X.; Carrillo-Cabrera, W.; Zou, X.; Xiao, F.-S. *J. Am. Chem. Soc.* **2012**, *134*, 4557.

(48) Moteki, T.; Chaikittisilp, W.; Shimojima, A.; Okubo, T. *J. Am. Chem. Soc.* **2008**, *130*, 15780.

(49) Varoon, K.; Zhang, X.; Elyassi, B.; Brewer, D. D.; Gettel, M.; Kumar, S.; Lee, J. A.; Maheshwari, S.; Mittal, A.; Sung, C.-Y.; Cococcioni, M.; Francis, L. F.; McCormick, A. V.; Mkhoyan, K. A.; Tsapatsis, M. *Science* **2011**, *333*, 72.

(50) Corma, A. *Chem. Rev.* **1997**, *97*, 2373.

(51) Christiansen, S. C.; Zhao, D.; Janicke, M. T.; Landry, C. C.; Stucky, G. D.; Chmelka, B. F. *J. Am. Chem. Soc.* **2001**, *123*, 4519.

(52) Choi, M.; Na, K.; Kim, J.; Sakamoto, Y.; Terasaki, O.; Ryoo, R. *Nature* **2009**, *461*, 246.

(53) Na, K.; Jo, C.; Kim, J.; Cho, K.; Jung, J.; Seo, Y.; Messinger, R. J.; Chmelka, B. F.; Ryoo, R. *Science* **2011**, *333*, 328.

(54) Zhang, X.; Liu, D.; Xu, D.; Asahina, S.; Cychosz, K. A.; Agrawal, K. V.; Al Wahedi, Y.; Bhan, A.; Al Hashimi, S.; Terasaki, O.; Thommes, M.; Tsapatsis, M. *Science* **2012**, *336*, 1684.

(55) Na, K.; Choi, M.; Park, W.; Sakamoto, Y.; Terasaki, O.; Ryoo, R. *J. Am. Chem. Soc.* **2010**, *132*, 4169.

(56) Almond, G. G.; Harris, R. K.; Graham, P. *J. Chem. Soc.-Chem. Commun.* **1994**, 851.

(57) Apperley, D. C.; Hudson, M. J.; Keene, M. T. J.; Knowles, J. A. *J. Mater. Chem.* **1995**, *5*, 577.

(58) Almond, G. G.; Harris, R. K.; Franklin, E. K.; Graham, P. *J. Mater. Chem.* **1996**, *6*, 843.

(59) Almond, G. G.; Harris, R. K.; Franklin, K. R. *Solid State Nucl. Mag.* **1996**, *6*, 31.

(60) Gardiennet, C.; Tekely, P. *J. Phys. Chem. B* **2002**, *106*, 8928.

(61) Gardiennet, C.; Marica, F.; Fyfe, C. A.; Tekely, P. *J. Chem. Phys.* **2005**, *122*, 054705.

(62) Engelhardt, G. In *Encyclopedia of NMR*; Grant, D. M., Harris, R. K., Eds.; Wiley: New York, 1995.

(63) Fyfe, C. A.; Gies, H.; Feng, Y. *J. Chem. Soc., Chem. Commun.* **1989**, 1240.

(64) Fyfe, C. A.; Gies, H.; Feng, Y.; Kokotailo, G. T. *Nature* **1989**, *341*, 223.

(65) Fyfe, C. A.; Grondey, H.; Feng, Y.; Kokotailo, G. T. *J. Am. Chem. Soc.* **1990**, *112*, 8812.

(66) Brouwer, D. H.; Darton, R. J.; Morris, R. E.; Levitt, M. H. *J. Am. Chem. Soc.* **2005**, *127*, 10365.

(67) Brouwer, D. H. *J. Am. Chem. Soc.* **2008**, *130*, 6306.

(68) Brouwer, D. H. *J. Magn. Reson.* **2008**, *194*, 136.

(69) Cadars, S.; Brouwer, D. H.; Chmelka, B. F. *Phys. Chem. Chem. Phys.* **2009**, *11*, 1825.

(70) Florian, P.; Fayon, F.; Massiot, D. *J. Phys. Chem. C* **2009**, *113*, 2562.

(71) Bull, L. M.; Bussemer, B.; Anupold, T.; Reinhold, A.; Samoson, A.; Sauer, J.; Cheetham, A. K.; Dupree, R. *J. Am. Chem. Soc.* **2000**, *122*, 4948.

(72) Xue, X. Y.; Kanzaki, M. *Solid State Nucl. Mag.* **2000**, *16*, 245.

(73) Peng, L. M.; Liu, Y.; Kim, N. J.; Readman, J. E.; Grey, C. P. *Nat. Mater.* **2005**, *4*, 216.

(74) Huo, H.; Peng, L. M.; Gan, Z. H.; Grey, C. P. *J. Am. Chem. Soc.* **2012**, *134*, 9708.

(75) Sklenak, S.; Dedecek, J.; Li, C. B.; Wichterlova, B.; Gabova, V.; Sierka, M.; Sauer, J. *Angew. Chem.-Int. Edit.* **2007**, *46*, 7286.

(76) Brouwer, D. H.; Enright, G. D. *J. Am. Chem. Soc.* **2008**, *130*, 3095.

(77) Kristiansen, P. E.; Carravetta, M.; Lai, W. C.; Levitt, M. H. *Chem. Phys. Lett.* **2004**, *390*, 1.

(78) Cadars, S.; Lesage, A.; Hedin, N.; Chmelka, B. F.; Emsley, L. *J. Phys. Chem. B* **2006**, *110*, 16982.

(79) Hodgkinson, P.; Holmes, K. J.; Hore, P. J. *J. Magn. Reson., Ser. A* **1996**, *120*, 18.

(80) Pham, T. N.; Griffin, J. M.; Masiero, S.; Lena, S.; Gottarelli, G.; Hodgkinson, P.; Fillip, C.; Brown, S. P. *Phys. Chem. Chem. Phys.* **2007**, *9*, 3416.

(81) Brouwer, D. H. *Solid State Nucl. Magn. Reson.*, **2013**, in press, doi: 10.1016/j.ssnmr.2013.01.003.

(82) Wolfram, S.; *Mathematica: A system for doing mathematics by computer*, version 6.0 ed.; Wolfram Media: Champaign, IL, 2007.

(83) Segall, M. D.; Lindan, P. J. D.; Probert, M. J.; Pickard, C. J.; Hasnip, P. J.; Clark, S. J.; Payne, M. C. *J. Phys.: Condens. Matter* **2002**, *14*, 2717.

(84) Clark, S. J.; Segall, M. D.; Pickard, C. J.; Hasnip, P. J.; Probert, M. J.; Refson, K.; Payne, M. C. *Z. Kristallogr.* **2005**, *220*, 567.

(85) Perdew, J. P.; Burke, K.; Ernzerhof, M. *Phys. Rev. Lett.* **1996**, *77*, 3865.

(86) Vanderbilt, D. *Phys. Rev. B* **1990**, *41*, 7892.

(87) Monkhorst, H. J.; Pack, J. D. *Phys. Rev. B* **1976**, *13*, 5188.

(88) Pickard, C. J.; Mauri, F. *Phys. Rev. B* **2001**, *63*, 245101.

(89) Yates, J. R.; Pickard, C. J.; Mauri, F. *Phys. Rev. B* **2007**, *76*, 024401.

(90) Frisch, M. J.; Trucks, G. W.; Schlegel, H. B.; Scuseria, G. E.; Robb, M. A.; Cheeseman, J. R.; Montgomery, J. A., Jr.; Vreven, T.; Kudin, K. N.; Burant, J. C.; Millam, J. M.; Iyengar, S. S.; Tomasi, J.; Barone, V.; Mennucci, B.; Cossi, M.; Scalmani, G.; Rega, N.; Petersson, G. A.; Nakatsuji, H.; Hada, M.; Ehara, M.; Toyota, K.; Fukuda, R.; Hasegawa, J.; Ishida, M.; Nakajima, T.; Honda, Y.; Kitao, O.; Nakai, H.; Klene, M.; Li, X.; Knox, J. E.; Hratchian, H. P.; Cross, J. B.; Bakken, V.; Adamo, C.; Jaramillo, J.; Gomperts, R.; Stratmann, R. E.; Yazyev, O.; Austin, A. J.; Cammi, R.; Pomelli, C.; Ochterski, J. W.; Ayala, P. Y.; Morokuma, K.; Voth, G. A.; Salvador, P.; Dannenberg, J. J.; Zakrzewski, V. G.; Dapprich, S.; Daniels, A. D.; Strain, M. C.; Farkas, O.; Malick, D. K.; Rabuck, A. D.; Raghavachari, K.; Foresman, J. B.; Ortiz, J. V.; Cui, Q.; Baboul, A. G.; Clifford, S.; Cioslowski, J.; Stefanov, B. B.; Liu, G.; Liashenko, A.; Piskorz, P.; Komaromi, I.; Martin, R. L.; Fox, D. J.; Keith, T.; Al-Laham, M. A.; Peng, C. Y.; Nanayakkara, A.; Challacombe, M.; Gill, P. M. W.; Johnson, B.; Chen, W.; Wong, M. W.; Gonzalez, C.; Pople, J. A. *Gaussian 03*; Gaussian Inc.: Wallingford CT, 2004.

(91) Ditchfield, R. *Mol. Phys.* **1974**, *27*, 789.

(92) Jensen, F. *J. Chem. Theory Comput.* **2006**, *2*, 1360.

(93) Feller, D. *J. Comput. Chem.* **1996**, *17*, 1571.

(94) Schuchardt, K. L.; Didier, B. T.; Elsethagen, T.; Sun, L. S.; Gurumoorthi, V.; Chase, J.; Li, J.; Windus, T. L. *J. Chem Inf. Model.* **2007**, *47*, 1045.

(95) *Computational Chemistry Grid* (2008); http://www.gridchem.org.

(96) Dooley, R.; Allen, G.; Pamidighantam, S. In Proceedings from 13th Annual Mardi Gras Conference, Louisiana State University, Baton Rouge, LA, February 3–5, 2005; Center for Computation and Technology: Baton Rouge, LA, 2005, p 83.

(97) Milfeld, K.; Guiang, C.; Pamidighantam, S.; Giuliani, J. In *2005 Linux Clusters: The HPC Revolution* 2005.

(98) The distances observed in the TEM image of Figure 2 are somewhat smaller than the corresponding distances derived from PXRD (Figure 1), which is attributed to reduced interlayer spacing that is expected to result from partial decomposition of the organic species in the intense electron beam or from the partial extraction of surfactant molecules during the preparation of the TEM sample in ethanol.

(99) This is the estimated upper range of distances to which the dipolar recoupling experiment is expected to be sensitive. Previous studies on zeolites have shown that no significant differences in the buildup curves are observed for cutoff values >8 Å.

(100) Baerlocher, C.; McCusker, L. B.; Olson, D. H. *Atlas of Zeolite Framework Types*; 6th ed.; Elsevier: Amsterdam, 2007.

(101) Rietveld, H. M. *J. Appl. Crystallogr.* **1969**, *2*, 65.

(102) Baerlocher, C.; Hepp, A.; Meier, W. M. *DLS-76: A Program for the Simulation of Crystal Structures by Geometry Refinement*; Institute of Geochemistry and Petrology, ETH: Zurich, 1978.

(103) Cadars, S.; Mifsud, N.; Lesage, A.; Epping, J. D.; Hedin, N.; Chmelka, B. F.; Emsley, L. *J. Phys. Chem. C* **2008**, *112*, 9145.

(104) Brown, S. P.; Perez-Torralba, M.; Sanz, D.; Claramunt, R. M.; Emsley, L. *Chem. Commun.* **2002**, 1852.

(105) Lai, W. C.; McLean, N.; Gansmüller, A.; Verhoeven, M. A.; Antonioli, G. C.; Carravetta, M.; Duma, L.; Bovee-Geurts, P. H. M.; Johannessen, O. G.; de Groot, H. J. M.; Lugtenburg, J.; Emsley, L.; Brown, S. P.; Brown, R. C. D.; DeGrip, W. J.; Levitt, M. H. *J. Am. Chem. Soc.* **2006**, *128*, 3878.

(106) Massiot, D.; Fayon, F.; Deschamps, M.; Cadars, S.; Florian, P.; Montouillout, V.; Pellerin, N.; Hiet, J.; Rakhmatullin, A.; Bessada, C. *C. R. Chim.* **2010**, *13*, 117.

(107) Brown, S. P.; Emsley, L. *J. Magn. Reson.* **2004**, *171*, 43.

(108) Pileio, G.; Guo, Y.; Pham, T. N.; Griffin, J. M.; Levitt, M. H.; Brown, S. P. *J. Am. Chem. Soc.* **2007**, *129*, 10972.

(109) Pileio, G.; Mamone, S.; Mollica, G.; Montesinos, I. M.; Gansmuller, A.; Carravetta, M.; Brown, S. P.; Levitt, M. H. *Chem. Phys. Lett.* **2008**, *456*, 116.

(110) Ramsey, N. F. *Phys. Rev.* **1953**, *91*, 303.

(111) The accuracy of DFT calculations of $^2J(^{29}Si{-}O{-}^{29}Si)$ couplings using cluster approaches is expected to be significantly lower for $^{29}Si{-}O{-}^{29}Si$ site pairs involving $Q^3$ Si moieties, because the local environments of $Q^3$ $^{29}Si$ moieties are typically difficult to model accurately in these systems.

(112) Treacy, M. M. J.; Foster, M. D.; Randall, K. H. *Micropor. Mesopor. Mat.* **2006**, *87*, 255.

(113) Delgado-Friedrichs, O.; O'Keeffe, M. *J. Solid State Chem.* **2005**, *178*, 2480.

(114) The inability of DFT calculations to converge towards a single unique structure when starting from the very similar sets of initial Si positions of candidate structures **3** and **4** is likely due to an important current modeling limitation: charge-compensating surfactant and/or adsorbed solvent molecules are not accounted for, requiring the use of protonated $Q^3$ Si atoms to compensate the resulting local charge deficits. In the course of optimization, silanol hydrogen atoms tend to form hydrogen bonds to nearby oxygen atoms, distorting the local environments of $Q^3$ sites Si1 and Si2, and to a lesser extent those of $Q^4$ sites Si3, Si4, and Si5 with respect to a fully nonprotonated structure.

(115) The distance constraints are still satisfied because of the strong similarity between the experimental DQ curves that need to be interchanged as a result of the interchange of sites 1↔2 and 3↔4 (e.g., 1-3 ↔ 2-4 or 3-5 ↔ 4-5, etc.)

(116) Fyfe, C. A.; Feng, Y.; Gies, H.; Grondey, H.; Kokotailo, G. T. *J. Am. Chem. Soc.* **1990**, *112*, 3264.

(117) Cadars, S.; Smith, B. J.; Epping, J. D.; Acharya, S.; Belman, N.; Golan, Y.; Chmelka, B. F. *Phys. Rev. Lett.* **2009**, *103*, 136802.

(118) Webber, A. L.; Elena, B.; Griffin, J. M.; Yates, J. R.; Pham, T. N.; Mauri, F.; Pickard, C. J.; Gil, A. M.; Stein, R.; Lesage, A.; Emsley, L.; Brown, S. P. *Phys. Chem. Chem. Phys.* **2010**, *12*, 6970.

(119) Fyfe, C. A.; Strobl, H.; Kokotailo, G. T.; Kennedy, G. J.; Barlow, G. E. *J. Am. Chem. Soc.* **1988**, *110*, 3373.

(120) Brenn, U.; Ernst, H.; Freude, D.; Herrmann, R.; Jähnig, R.; Karge, H. G.; Kärger, J.; Köning, T.; Mädler, B.; Pingel, U.-T.; Prochnow, D.; Schwiger, W. *Microporous Mesoporous Mater.* **2000**, *40*, 43.

(121) Joyce, S. A.; Yates, J. R.; Pickard, C. J.; Mauri, F. *J. Chem. Phys.* **2007**, *127*, 204107.